coatings

MDPI

Article

Effect of Annealing Temperature on Radio Frequency Sputtered p-Type Delafossite Copper Chromium Oxide ($CuCrO_2$) Thin Films and Investigation of Diode Characteristics Forming Transparent pn-Heterojunction

Sreeram Sundaresh *, Akash Hari Bharath and Kalpathy B. Sundaram

Department of Electrical and Computer Engineering, University of Central Florida, Orlando, FL 32826, USA
* Correspondence: sreeram.sundaresh@knights.ucf.edu

Abstract: For the first time, the deposition of $CuCrO_2$ thin films was carried out using a dual-target RF magnetron sputtering technique using Cu_2O and Cr_2O_3 targets. The deposited films were subsequently annealed in N_2 ambiance from 600–900 °C. This work reports that the electrical, optical, structural, and morphological properties of $CuCrO_2$ thin films are significantly affected due to the variation in the annealing temperature. XRD analysis confirms the presence of single-phase $CuCrO_2$ in the films annealed at 650 °C. The presence of Cu in the 1+ oxidation state in the phase pure $CuCrO_2$ thin films was confirmed through XPS analysis. Further, through XPS analysis, the oxidation states of Cu and Cr, the full-width half maximum (FWHM), the peak positions, and their respective binding energies have been elucidated. SEM analysis confirms the promotion of nanocrystalline growth in the thin films as the annealing temperature was increased from 600 °C. The average grain size increased from 40.22 nm to 105.31 nm as the annealing temperature was increased from 600 to 900 °C. Optical studies conducted in the wavelength range of 200 nm to 800 nm revealed a decrease in the optical transmission and optical bandgap with an increase in the annealing temperature. The highest optical transmission of ~81% and an optical bandgap of 3.21 eV were obtained for the films depicting the delafossite nature of $CuCrO_2$. The optical bandgap was found to vary between 3.16 eV and 3.74 eV for the films studied in this research. The lowest resistivity of 0.652 Ω cm was obtained for the films annealed at 650 °C. Transparent heterojunction diodes involving p-type delafossite copper chromium oxide ($CuCrO_2$) and n-type indium tin oxide (ITO) were fabricated. The best diode depicted a cut-in voltage of 0.85 V, a very low leakage current of 1.24 x 10-8, an ideality factor of 4.13, and a rectification ratio of 2375.

Keywords: delafossite $CuCrO_2$; heterojunction; pn-junction; diodes; RF sputtering; annealing studies; transparent diode; transparent heterojunction; p-type delafossite; thin films; electrical study; optical study; $CuCrO_2$ transmission; $CuCrO_2$ bandgap; $CuCrO_2$ resistivity; $CuCrO_2$ heterojunction; $CuCrO_2$ diode; p-$CuCrO_2$; n-ITO; p-$CuCrO_2$/n-ITO; $CuCrO_2$ XRD; $CuCrO_2$ XPS; $CuCrO_2$ SEM

Citation: Sundaresh, S.; Bharath, A.H.; Sundaram, K.B. Effect of Annealing Temperature on Radio Frequency Sputtered p-Type Delafossite Copper Chromium Oxide ($CuCrO_2$) Thin Films and Investigation of Diode Characteristics Forming Transparent pn-Heterojunction. *Coatings* **2023**, *13*, 263. https://doi.org/10.3390/coatings13020263

Academic Editor: Zhongkai Cheng

Received: 27 December 2022
Revised: 16 January 2023
Accepted: 19 January 2023
Published: 22 January 2023

1. Introduction

Transparent conducting oxides (TCOs) have attracted significant attention in recent years since they are a unique class of compounds that combine the properties of being transparent and electrically conducting at the same time [1]. TCOs are semiconductors that exhibit a large bandgap and a high optical transmission in the visible wavelength region [2,3]. Owing to these properties, TCOs find applications in optoelectronic devices, light-emitting diodes, solar cells, and transparent thin-film transistors [2,4–7]. TCOs have been extensively researched recently since their properties can be precisely controlled by varying their synthesis parameters. By precisely controlling the doping, TCOs such as SnO_2, In_2O_3, and ZnO can depict the electrical properties of a metal, semiconductor, or insulator while maintaining optical transparency [8–11]. Some of the well-known n-type

TCOs include Sn-doped In_2O_3 (ITO) [12–14], Sc-doped ZnO [15,16], SnO_2 [17,18], Al-doped ZnO (AZO) [19–23], and $CdSnO_2$ [24–26].

A combination of p- and n-type transparent conducting channels are used as active layers in transparent optoelectronic devices. Thus, it is mandatory to have a p-type counterpart. However, p-type TCOs have been identified to have either a good optical transparency (>80%) or a low electrical resistivity (<10^{-2} Ω-cm) [1,2]. It has been difficult to synthesize p-type TCOs with both of the aforementioned properties. The root cause of this can be attributed to the intrinsic electronic structure of metal oxides, where strongly localized O-2p orbitals occupy most of the top of the valence band [27,28]. It has been shown that the valence band level of metal oxides is far lower lying than that of metals, which can be resolved by doping [29]. However, the highly electronegative O_2 ions attract the holes, inhibiting their movement across the crystal lattice. Due to this, the localized holes need significant energy to cross the high barrier height to move across the crystal lattice [4]. This is the prime reason for the reduced electrical conductivity in p-type TCOs [30,31].

To alleviate this issue, a new concept of 'Chemical Modulation of Valence Band (CMVB)' was proposed by Hosono et al. [27]. They identified that the hybridization of O-2p orbitals is possible by the addition of appropriate cations such as Cu+. The reason stated that, since the energy level difference between Cu $3d^{10}$ and O $2p^6$ is very small, the former forms a strong covalent bond with the latter. During this process, the low-lying O-2p energy level is raised and the coulombic force of attraction between the oxygen ions and holes is reduced, which results in a lower energy requirement for holes to cross the barrier height. This ultimately results in an improvement in the electrical conductivity of p-type TCOs [29]. It was also reported by Zhang et al. that the thin films obtained using the CMVB technique preserves the optical transparency for visible light since it was noticed that the closed shell of $3d^{10}$ prevents the coloration of the deposited films [30].

Thin films that are obtained using the CMVB technique are called delafossites. The appropriate cation addition during the CMVB process could include either Ag+ or Cu+. However, the previous literature has shown that the delafossites obtained using Ag+ cation had a very high electrical resistivity (10^4 to 10^6 Ω-cm) [32]. This is due to the very low mobility of carriers which is a result of an unfavorable energy match between O-p and Ag-4d levels [33]. The delafossites obtained using the addition of Cu+ cation are called Cu-based delafossites, which have a chemical formula of $CuMO_2$, where Cu is the positive monovalent cation (Cu^+), M = Al^{3+}, Cr^{3+}, In^{3+}, Ga^{3+}, Sc^{3+}, and Y^{3+} (trivalent cation), and oxygen is the divalent anion (O^{2-}) [34]. This understanding provided a new dimension that led to a recent spike in the interest in p-type TCOs, particularly Cu-based delafossites [35–37]. It has been identified that Cu-based delafossites typically possess a high optical transparency (60%–85%) and a low electrical resistivity (5×10^{-2} to 8×10^{-3} Ω-cm) [31,38].

Among the p-type Cu-based delafossite candidates, $CuCrO_2$ is a promising material to be considered for transparent electronics applications since it presents a valuable trade-off between its optical and electrical properties [31,38]. $CuCrO_2$ has been reported to have a low synthesis temperature and acceptable thermal stability in the air [31,39]. The room temperature resistivity of RF magnetron sputtered $CuCrO_2$ has been previously reported to be 0.66 Ω cm with a transmittance of ~60% [40]. Hence, the $CuCrO_2$-based p-type delafossite structure was chosen as the material of research for this work.

In this research, the delafossite structure of $CuCrO_2$ was obtained for the first time using the dual-target RF magnetron sputtering technique of Cu_2O and Cr_2O_3 targets. The RF sputtering powers of Cu_2O and Cr_2O_3 targets were kept constant at 50 W and 200 W, respectively. Post-deposition, all the films were subjected to varying annealing temperatures in N_2 ambiance which enabled the formation of single-phase p-type $CuCrO_2$ delafossite thin films. The effect of an annealing temperature variation in the electrical, optical, structural, and morphological properties of the films has been investigated in this work. The superior optical and electrical characteristics of the phase pure $CuCrO_2$ thin films instigated the research on the heterojunction studies using p-$CuCrO_2$ and n-ITO as the active layers in this work.

2. Experimental Section

Deposition of $CuCrO_2$ thin film. In this work, the radio frequency (RF) magnetron sputtering technique was adopted for the deposition of $CuCrO_2$ thin films. An AJA international ultra-high vacuum three-gun sputtering equipment was utilized for the deposition of the films analyzed in this research. The film depositions were carried out on fused quartz substrates. Before the film deposition, all the quartz substrates were cleaned with acetone, methanol, DI water, and blow-dried with nitrogen gas. A dual target RF magnetron sputtering technique from 3-inch diameter targets of Cu_2O (99.99% purity, Maideli Advanced Materials Co., Ltd., Jiangying, China) and Cr_2O_3 (99.99% purity, Maideli Advanced Materials Co., Ltd., Jiangying, China) was employed to deposit 125 nm thick $CuCrO_2$ thin films. Two separate RF sources (13.56 MHz) were put to use for the sputtering of the targets. The RF power to the Cr_2O_3 was maintained at 200 W, whereas the RF power to the Cu_2O target was held constant at 50 W. All the depositions were performed only after the base chamber pressure reached 5×10^{-7} Torr. The deposition parameters maintained during this work for $CuCrO_2$ thin films have been listed in Table 1. To ensure a uniform film thickness, the substrate holder was rotated at a constant speed of 20 rpm. The film depositions were carried out at 400 °C (sputtering tool limit) and were subsequently annealed in a tube furnace at varying annealing temperatures from 600 °C to 900 °C in N_2 ambiance for 4 h. The N_2 flow rate was held constant at 300 sccm for all the post-deposition annealing. The annealing temperatures were decided based on earlier research which suggested that the delafossite phase of $CuCrO_2$ can be formed at a much lower temperature of ~ 600 °C [41–46]. Further, the final annealing temperature of 900 °C was chosen as the film started to appear hazy and patchy above 900 °C, leading to a decrease in the optical transmittance.

Table 1. Deposition parameters maintained during deposition of $CuCrO_2$ thin films.

Deposition Parameter	Specification
Sputtering gases	Ar
Base pressure	5×10^{-7} Torr
Deposition pressure	10 mTorr
RF power (Cr_2O_3)	200 W
RF power (Cu_2O)	50 W
Substrate temperature	400 °C
Sputtering gas flow rate	10 sccm
Thickness	125 nm
Annealing temperatures	600 °C, 650 °C, 750 °C, 800 °C, 900 °C
Annealing gas and flow rate	N_2 at 300 sccm

The aforementioned parameters were maintained for the deposition of a 200 nm p-layer in the p-$CuCrO_2$/n-ITO heterojunction. The deposition of ITO used as the n-layer in the heterojunction involved the use of a 2-inch diameter ITO sputtering target (Composition: 90% In_2O_3, 10% SnO_2, 99.99% purity, ACI alloys, Inc.) in an ultra-pure grade Ar ambiance. The distance between the target and the substrate was maintained at 5 cm. A 400 nm thick ITO layer was used as the n-layer in the heterojunction study. The deposition parameters maintained for the sputtering of the ITO target have been listed in Table 2. The aluminum contact pads in this research work have been deposited using the thermal evaporation technique.

Table 2. Deposition parameters maintained during deposition of ITO thin films.

Deposition Parameter	Specification
Sputtering gases	Ar
Base pressure	1×10^{-5} Torr
Deposition pressure	10 mTorr
RF power	100 W
Substrate temperature	Room Temperature
Gas flow	10 sccm
Thickness	400 nm

Film Characterization. The thickness of the deposited films was checked using the Veeco Dektak 150 Surface Profiler. XRD analysis was carried out using a PANalytical Empyrean XRD system (Malvern Panalytical, Westborough, MA, USA), using radiation from a Cu source at 45 kV and 40 mA. The diffraction patterns recorded between 2θ angles of 25 and 70° assisted in the identification of the materials. Further, the phase information was analyzed using HighScore Plus Software (Malvern Panalytical, Westborough, MA, USA). ESCALAB 250 Xi + X-ray photoelectron spectroscopy (XPS) (ThermoFisher Scientific, Waltham, MA, USA) with a monochromatic Al Kα source (1486.7 eV) was used to determine the elemental composition of the films and the oxidation states of the elements. Prior to the XPS analysis, a surface oxide removal was carried out by the ion beam milling of the film surface using an in-built EX06 ion source. Thermo Fischer Scientific Avantage software (v5.9902) was used to perform elemental composition analyses, functional group analyses, and XPS peak fitting. Zeiss ULTRA-55 FEG SEM (Zeiss Microscopy, White Plains, NY, USA) was used to evaluate the surface morphology of the post-deposition annealed films. The optical transmission was measured using a Cary 100 UV-IR Spectrophotometer (Varian Analytical Instruments, Walnut Creek, CA, USA) at light wavelengths from 200 nm to 800 nm. The transmission data were used to conduct the bandgap studies of the films with the help of the Tauc plot. The hot probe method and four-point probe (Magne-tron Instruments Model M-700) were used to check the conductivity type of the thin films post-annealing. To measure the resistivity of the post-deposition annealed thin films, the parallel aluminum contact pads were patterned as shown in Figure 1. A photolithography process was adopted to pattern the Al contact pad windows, which was followed by Al metal deposition using a thermal evaporation process and the removal of photoresist using the lift-off technique. The resistance (R) of the thin films was calculated using the IV characteristics obtained from the Keithley 2450 source meter unit. The resistivity (ρ) of the thin films was identified using Equation (1):

$$\rho = R * \frac{A}{L} \quad (1)$$

where R is the resistance, L is the length, and A is the area of the cross-section.

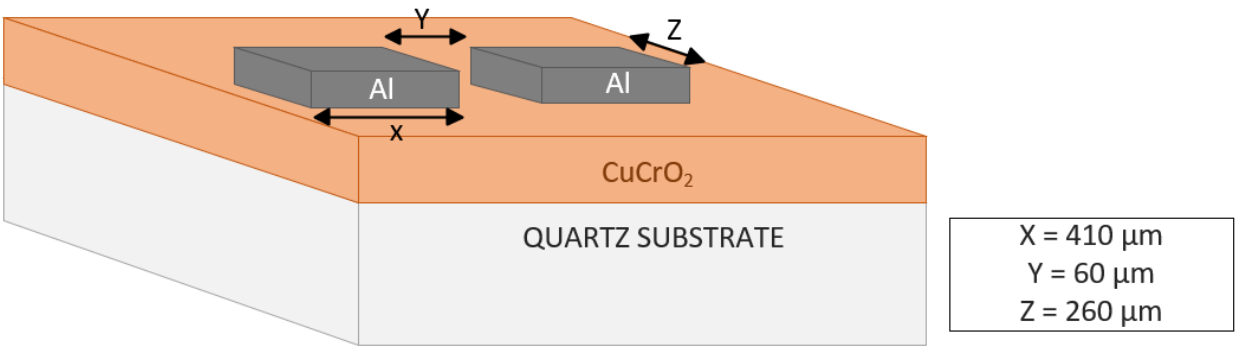

Figure 1. Diagrammatic representation of contact pads used for electrical measurements.

3. Results and Discussion

XRD analysis. The XRD diffractograms of the films annealed at temperatures ranging from 600 to 900 °C have been shown in Figure 2. Due to the use of quartz slides as substrates in this work, a broad amorphous quartz peak appeared in all the films at 2θ angles 18–25°. Hence, 2θ limits in Figure 2 have been adjusted to omit the amorphous peak of quartz. A higher annealing temperature of ~ 600 °C is required for a nanocrystalline growth in the films. This is evident from the amorphous nature of films obtained post-annealing at 500 °C. It also confirms that higher thermal energy is required for the crystallization of the deposited films. Prominent peaks start to appear at annealing temperatures of 600 °C and higher. At an annealing temperature of 600 °C, peaks pertaining to CuO (indicated as 'o' in Figure 2), Cr (indicated as '#' in Figure 2), and $CuCr_2O_4$ (indicated as '+' in Figure 2) were identified. However, the CuO and $CuCr_2O_4$ phases in the films are not acceptable for their use in TCO applications. Additionally, previous research has reported that a higher annealing temperature is required for the removal of CuO and $CuCr_2O_4$ phases and the promotion of $CuCrO_2$ phases in the films [35,43]. On a further increase in the annealing temperature to 650 °C, all the aforementioned peaks disappeared, leading to the promotion of the pure phase delafossite nature of $CuCrO_2$ (indicated as '*' in Figure 2) thin films. Further increases in the annealing temperatures led to the disintegration of the single-phase $CuCrO_2$. Additional peaks of Cr started to appear in the thin films annealed at 750 °C along with $CuCrO_2$ peaks. Since Cr is characteristically a high-temperature species, the single-phase $CuCrO_2$ disintegrates and the Cr peak is observed at 750 °C, which appears as Cr_2O_3 with a further increase in the annealing temperature [47]. At 800 °C and 900 °C of annealing temperatures, Cr_2O_3 (indicated as '•' in Figure 2) peaks were identified in addition to $CuCrO_2$ peaks. It is worth mentioning that, since CuO and $CuCr_2O_4$ phases were not present in the films annealed above 600 °C, it is safe to conclude that both CuO and $CuCr_2O_4$ are comparatively lower temperature phases. The growth mechanism of $CuCrO_2$ can be attributed to the additive reaction between Cr_2O_3 and Cu_2O as shown in Equation (2) [48,49].

$$Cu_2O_{(s)} + Cr_2O_{3(s)} \rightarrow 2CuCrO_{2(s)} \quad (2)$$

The appearance of single-phase $CuCrO_2$ at annealing temperatures ~650 °C has been reported in previous works [41,43,46]. The diffraction peaks of the film annealed at 650 °C indexed well to the delafossite $CuCrO_2$ (ICDD: 98-016-3253) structure. The major diffraction peaks identified at 2θ angles of 31.343°, 35.186°, 36.377°, 40.845°, 55.812°, 62.353°, and 65.419^0 were indexed to (006), (101), (012), (104), (018), (110), and (1010) of $CuCrO_2$, respectively. As evident from Figure 2, an increase in the peak sharpness and peak intensity is confirmed as the annealing temperature is increased from 600 °C to 900 °C. This verifies a steady improvement in the crystallinity of the films with an increase in the annealing temperature. The XRD peaks identified using the diffractograms shown in Figure 2 have been listed in Table 3.

XPS Analysis. ESCALAB 250 Xi + X-ray photoelectron spectroscopy (XPS) (ThermoFisher Scientific, Waltham, MA, USA) with a monochromatic Al Kα source (1486.7 eV) was used to carry out the XPS study. The binding energy calibration was performed automatically by the spectrometer using the copper sample which was built into the instrument. Figure 3a shows the recorded XPS survey spectra of the $CuCrO_2$ thin film obtained at an annealing temperature of 650 °C. The phase purity of the films can be confirmed as only peaks corresponding to Cu, Cr, and O were identified from the survey spectrum. The survey spectrum also shows the identified Auger peaks of Cu and O. Cu-2p, Cr-2p, and O-1s core level spectrums have been resolved and shown in Figure 3b–d, respectively. The core level spectrums, oxidation states, bonding configurations, full-width half maximum (FWHM), peak positions, satellite peak positions, and their respective binding energy have been calculated and reported in Table 4. Copper chromium oxide essentially exists in two phases: $CuCr_2O_4$ (spinal structure) and $CuCrO_2$ (delafossite structure) [48,50]. Previous research has shown that the oxidation state of Cu in $CuCrO_2$ is 1+ while Cu exists in a

2+ oxidation state in $CuCr_2O_4$ [51]. The distinguishing feature between the core level spectra of the Cu^{1+} and Cu^{2+} species are the satellite peaks. In the case of the Cu^{2+} species, strong satellite peaks (shake-up satellite features) are observed, while they are completely absent for the Cu^{1+} species [51–54]. The presence of satellites has been attributed to the metal–ligand charge transfer that occurs during the photoemission process [55].

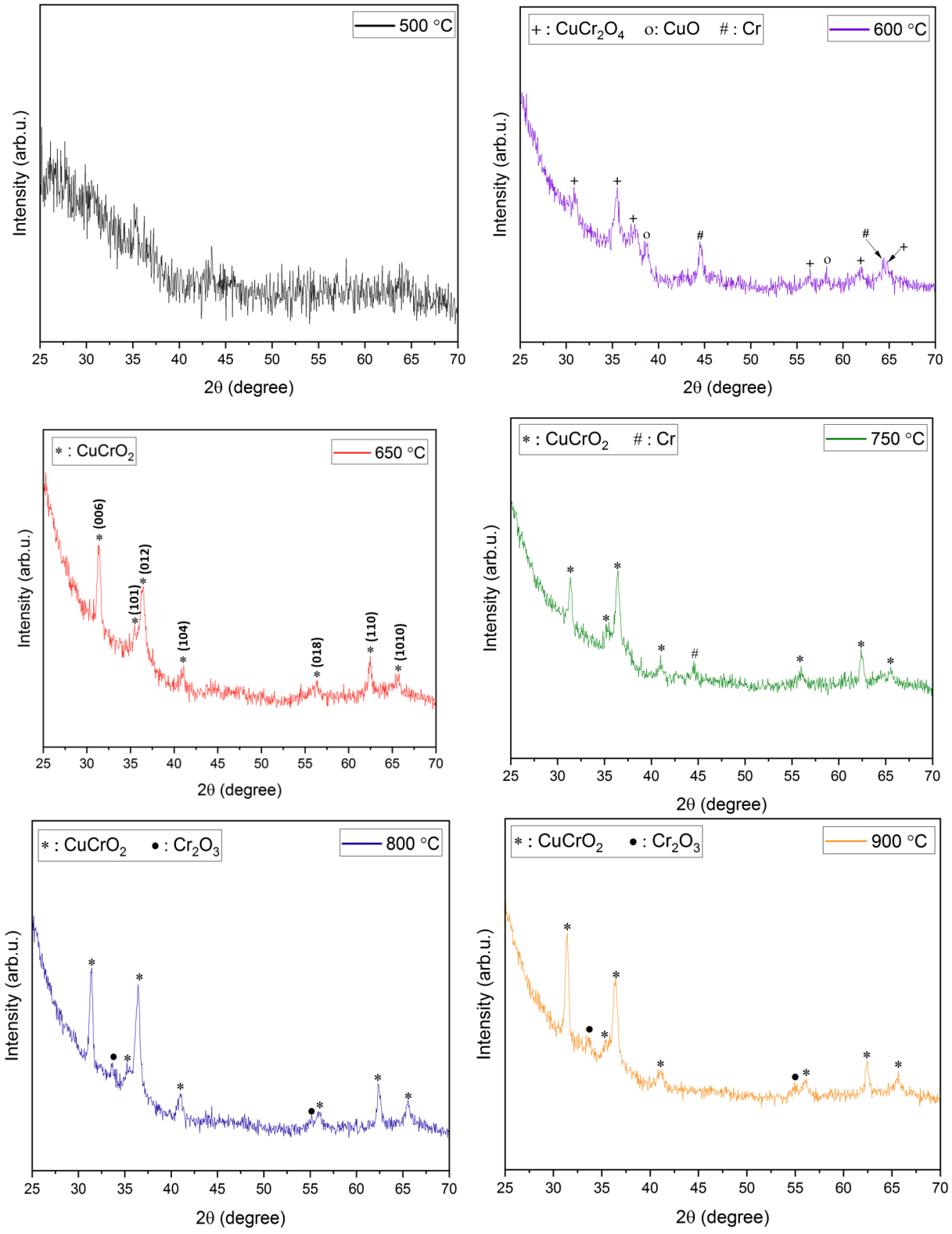

Figure 2. XRD diffractograms of films annealed at different temperatures.

Table 3. Relation between post-deposition annealing condition and phases identified through XRD analysis.

Annealing Temperature (°C)	Phases Identified
500	-
600	$Cr + CuO + CuCr_2O_4$
650	$CuCrO_2$ (delafossite)
750	$Cr + CuCrO_2$
800	$CuCrO_2 + Cr_2O_3$
900	$CuCrO_2 + Cr_2O_3$

The Cu-2p core level XPS spectrum has been shown in Figure 3b. Two separate spin-orbit components of Cu classified as the main peaks of Cu (marked as peak 1 and peak 2 in Figure 3b), Cu $2p_{1/2}$ and Cu $2p_{3/2}$ have been identified at 952.40 eV and 932.27 eV, respectively. The spin–orbit split energy for the Cu-2p core level reported in this work is $\Delta_{Cu\ 2p}$ = 20.13 eV. This result is close to the values previously reported in the literature for Cu existing in a 1+ oxidation state in $CuCrO_2$ phases [54,56]. It is important to note that there is an absence of satellite peaks corresponding to the Cu-doublet that appears towards the higher energy side of the main peaks. A similar absence of satellite peaks has been reported previously in the literature that report single-phase Cu-based delafossites [35,36,57].

The Cr-2p core level XPS spectrum has been shown in Figure 3c. The Cr-2p doublet, Cr $2p_{1/2,}$ and Cr $2p_{3/2}$ (marked as peaks 1 and 2 in Figure 3c) have been identified at 586.00 eV and 576.16 eV, respectively. The spin–orbit split energy for the Cr-2p core level obtained in this work is $\Delta_{Cr\ 2p}$ = 9.84 eV. This result is in good agreement with the previously reported values for Cr existing in a 3+ oxidation state in $CuCrO_2$ phases [52,54]. In the same range of the energies of the Cr core level spectrum, the Cu Auger peak (Cu LMM) is also identified. The Cu LMM peak is centered at 569.9 eV, which suggests the presence of Cu^{1+} rather than metallic Cu^{45}, which is centered at 568.3eV [49]. Similar findings were reported in the literature on the delafossite phase of $CuCrO_2$ [49,54,58].

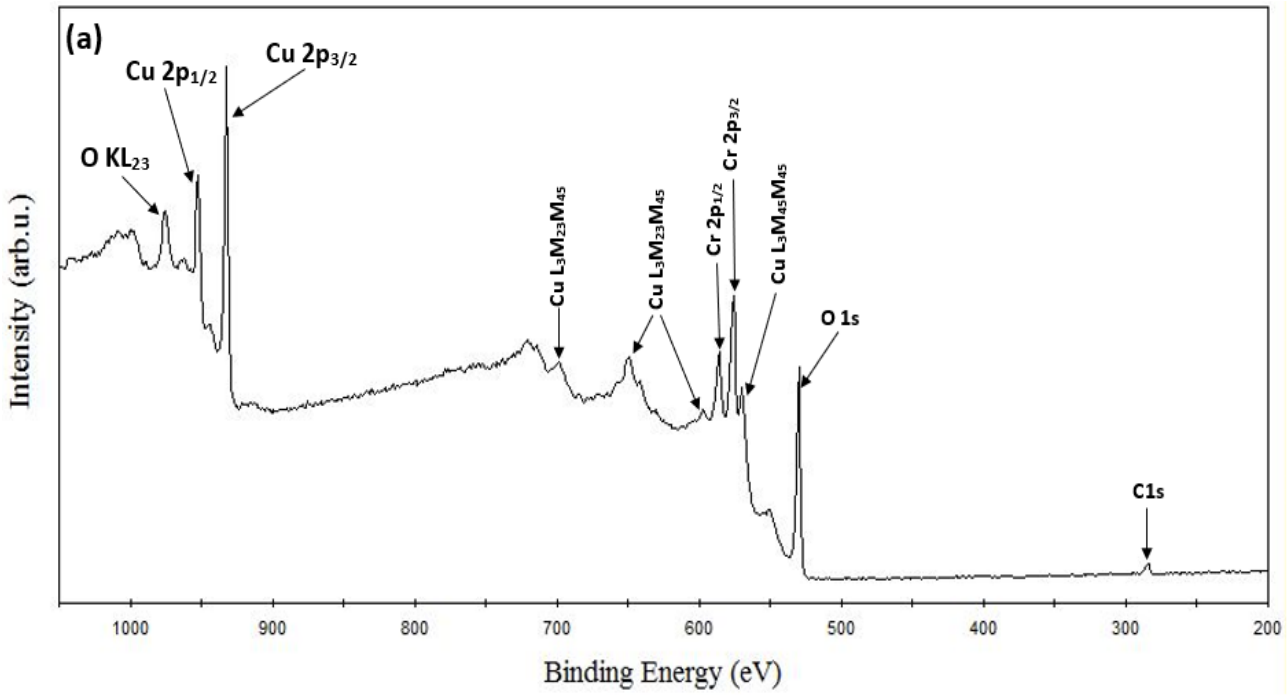

Figure 3. *Cont.*

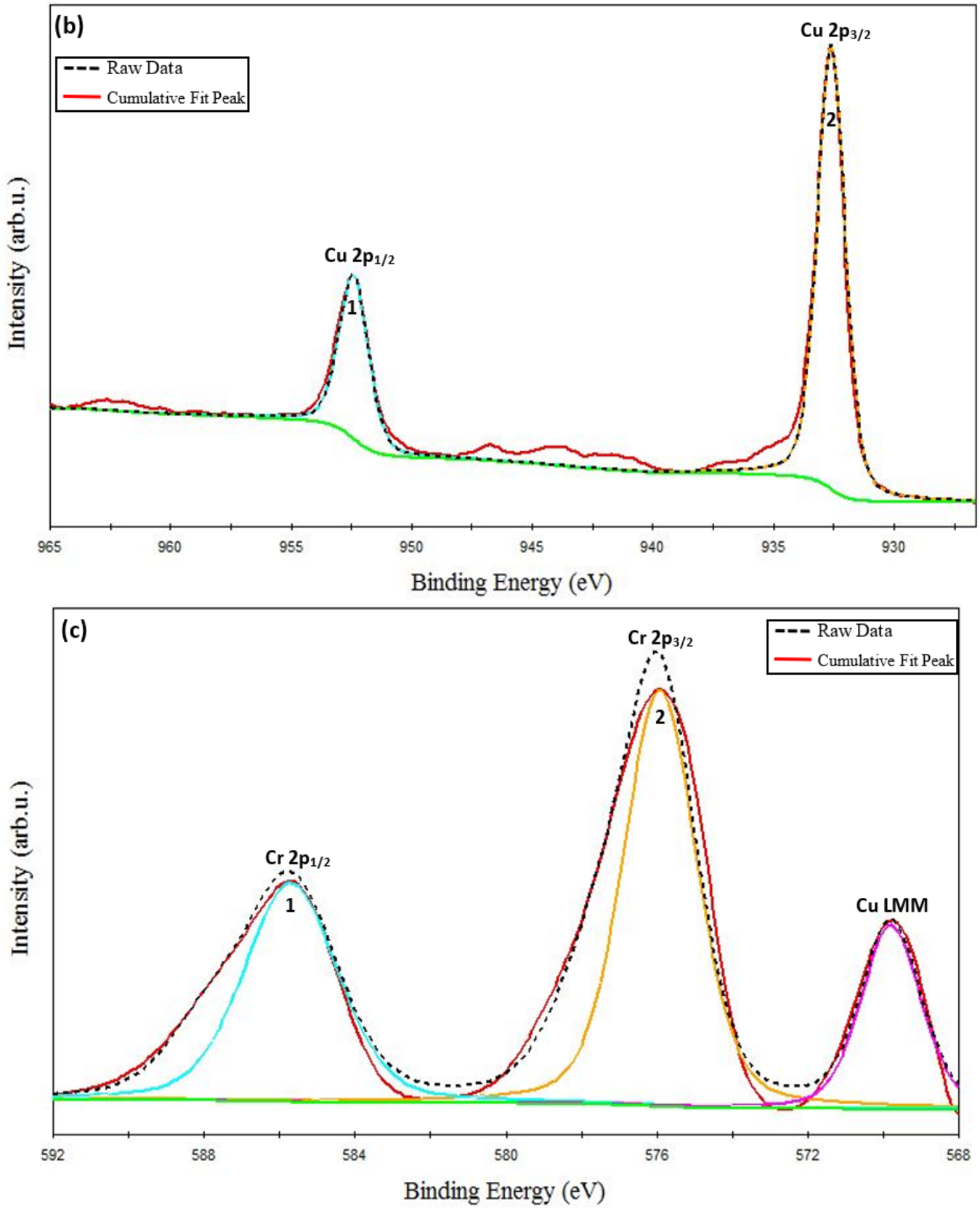

Figure 3. *Cont.*

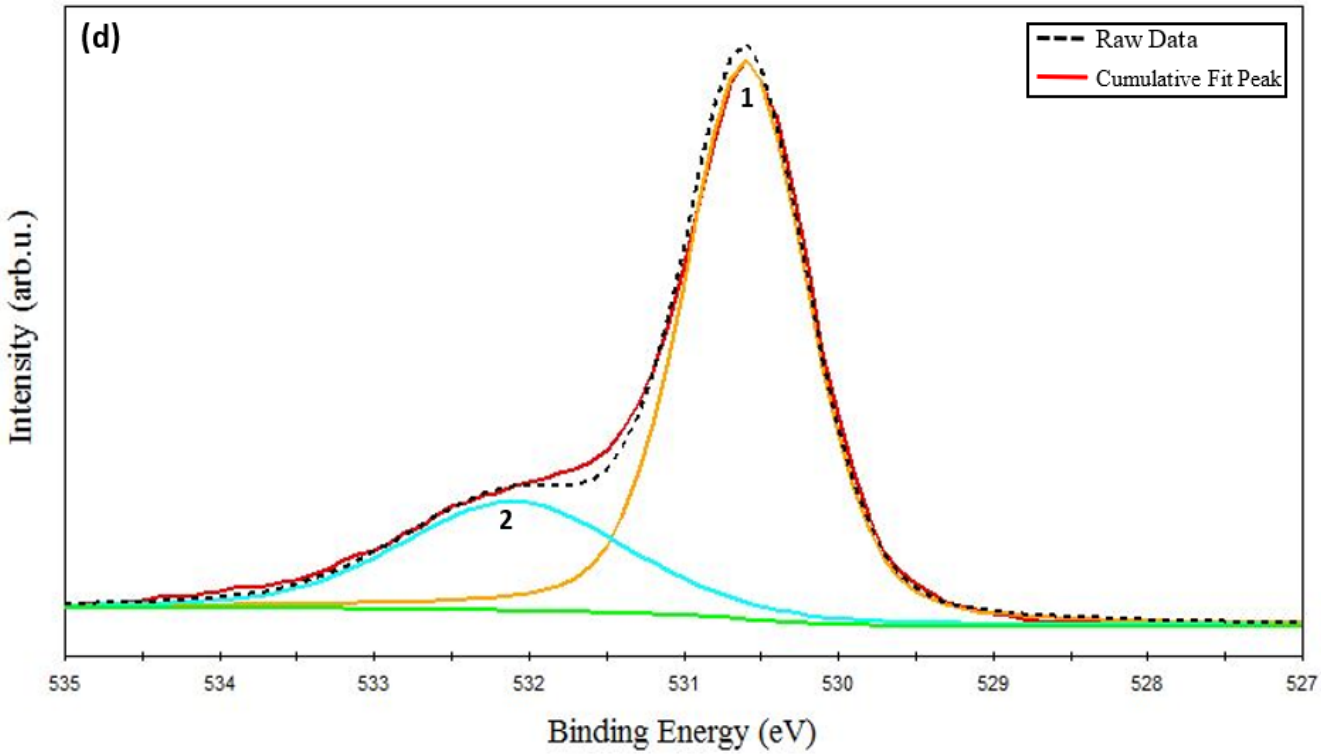

Figure 3. XPS spectra of $CuCrO_2$ film annealed at 650 °C: (**a**) survey spectrum, (**b**) Cu-2p, (**c**) Cr-2p, and (**d**) O-1s core level spectrum.

Table 4. Full-width half maximum (FWHM), peak positions, satellite peak positions, and their respective binding energy of $CuCrO_2$ film annealed at 650 °C.

Material	Peak	Oxidation State	Binding Energy (eV)	Satellite Peak (eV)	FWHM (eV)
$CuCrO_2$	Cu $2p_{3/2}$	Cu^{1+}	932.27 eV	-	3.52 eV
	Cu $2p_{1/2}$	Cu^{1+}	952.40 eV	-	1.56 eV
	Cr $2p_{3/2}$	Cr^{3+}	576.16 eV	-	4.45 eV
	Cr $2p_{1/2}$	Cr^{3+}	586.00 eV	-	3.43 eV

The resolved O-1s core level XPS spectrum has been shown in Figure 3d. The main O-1s peak is centered at 530.12 eV (marked as peak 1 in Figure 3d), which corresponds to lattice oxygen [49,59]. An energy-resolved O-1s peak identified at 532.08 eV (marked as peak 2 in Figure 3d) pertains to the chemisorbed oxygen. These results indicate that Cu and Cr cations mainly exist in the oxidation state of 1+ and 3+, respectively. With the help of XPS analysis and the XRD results, it can be asserted that the pure phase delafossite structure of $CuCrO_2$ was successfully synthesized at an annealing temperature of 650 °C.

Morphology Studies. Figure 4 shows the FESEM images at 50 K X magnification of the post-deposition annealed films obtained at varying annealing temperatures from 600 °C to 900 °C. A nanocrystalline growth has been confirmed through the FESEM images obtained for the aforementioned annealing temperatures, as clearly seen in Figure 4a–e. An increase in the average grain size with an increase in the annealing temperature can be noticed. As the thermal energy increased, the grains obtain enough energy to undergo coalescence, which ultimately increases the average grain size. The average grain size escalated from 40.22 nm for a 600 °C annealed film to 105.31 nm for a 900 °C annealed film. It can be seen that at lower annealing temperatures of 600 °C and 650 °C, the FESEM images show a smooth matrix with no visible cracks. However, as the annealing temperature is increased

above 650 °C, gaps start to appear between the grains due to higher thermal energy, which is also observed in the earlier literature [60,61]. At an annealing temperature of 900 °C, rod-like structures were observed along with increased grain sizes. Rod-like structures are a characteristic appearance of Cr_2O_3 nanostructures, as reported previously [62,63]. This explanation is in complete agreement with our XRD findings which report the presence of Cr_2O_3 with $CuCrO_2$ at an annealing temperature of 900 °C. It can be safely concluded that increments in the annealing temperature promote the average grain sizes in the films under study. Figure 5 shows the increasing trend of the average grain size with an increase in the annealing temperature.

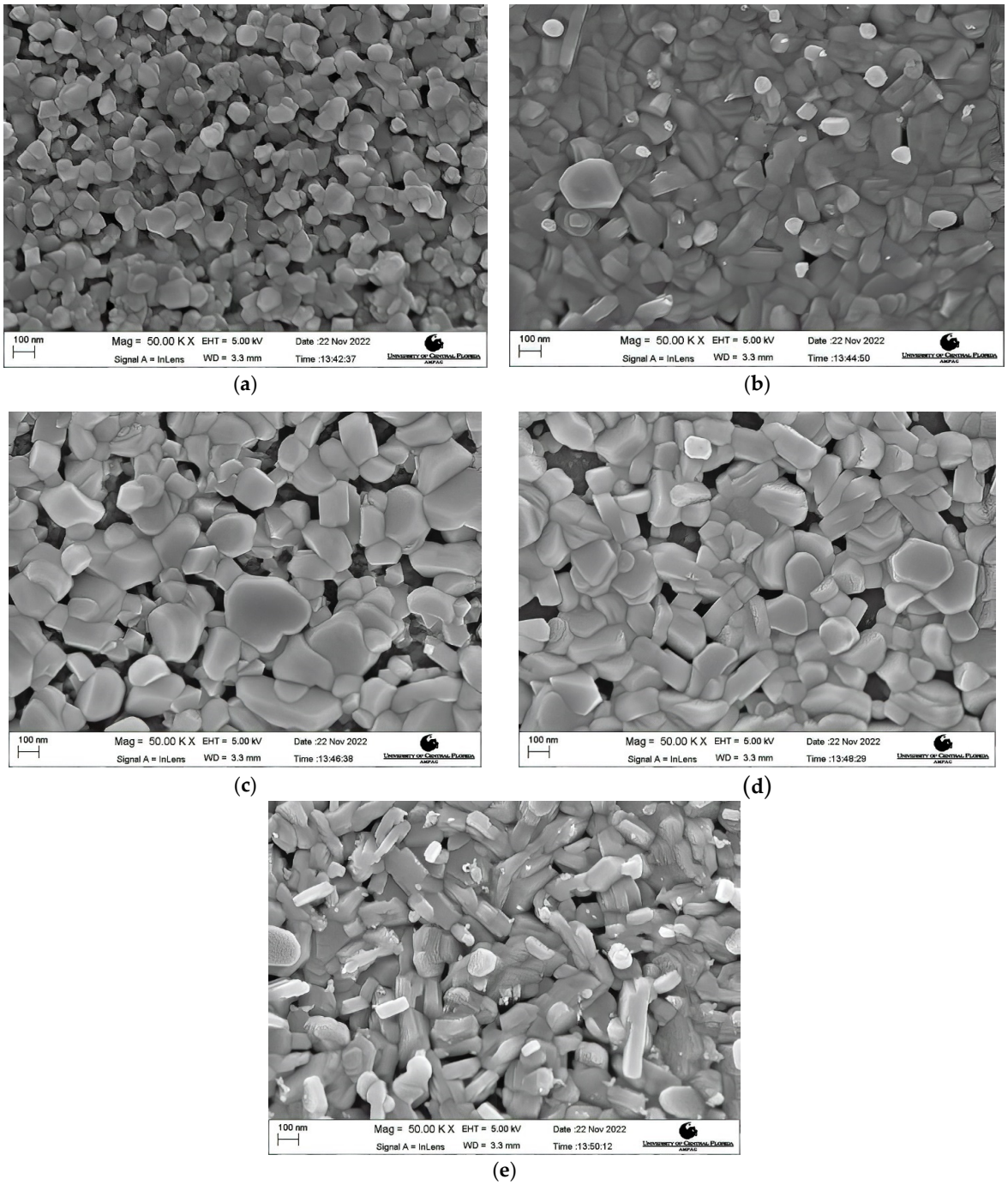

Figure 4. FESEM images of the films annealed at (**a**) 600 °C, (**b**) 650 °C, (**c**) 750 °C, (**d**) 800 °C, and (**e**) 900 °C.

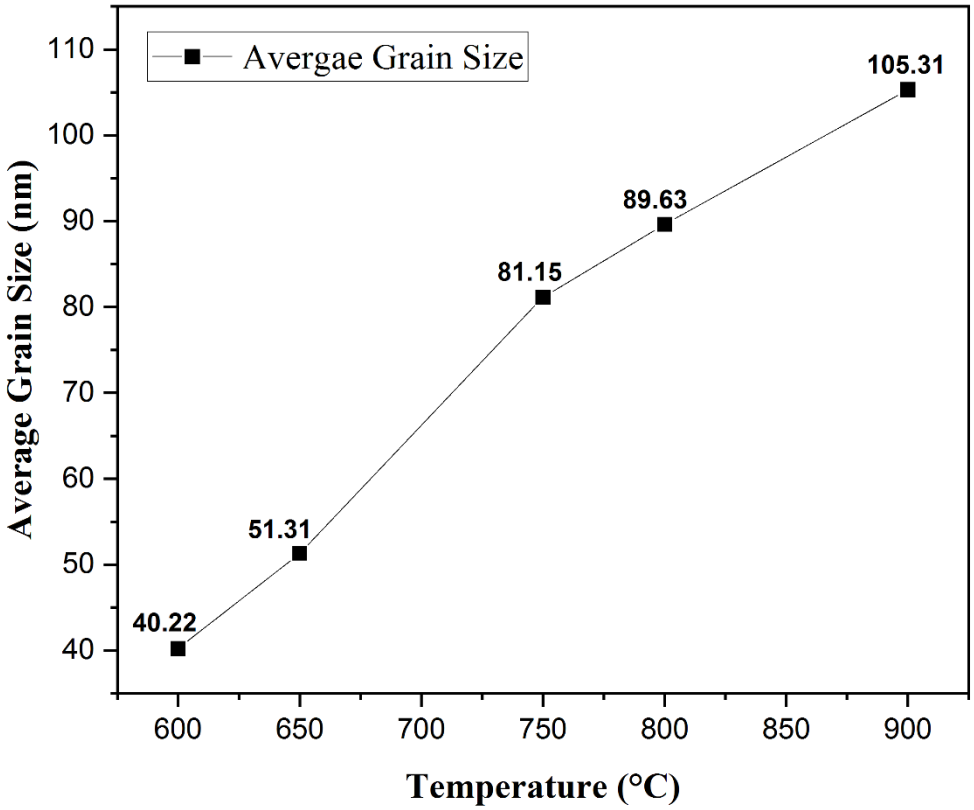

Figure 5. Relation between the average grain size and the annealing temperature.

Optical Studies—Optical Transmission. The optical transmission studies shown in Figure 6 were conducted on all the thin films deposited on quartz substrates. The transmission data had been recorded using a UV–Visible spectrophotometer for the wavelength range of 200–800 nm. It is worth mentioning that the transmission data are affected by the structural changes in the film and has a correlation with the results of the XRD analysis. It can be seen that the film annealed at 600 °C shows the lowest optical transmission. In contrast, the film annealed at 650 °C shows the highest optical transmission for the aforementioned wavelength range. As observed from the XRD analysis, CuO and $CuCr_2O_4$ phases are identified in the film annealed at 600 °C. This might be a reason for a decreased optical transmission in the 200–800 nm wavelength range. Similar findings have been reported previously [64,65]. An optical transmission value of ~45% is observed at a wavelength of 700 nm in the film annealed at 600 °C. The optical transmission increased extensively to ~81% at 700 nm as the annealing temperature was increased to 650 °C. This is due to the appearance of single-phase $CuCrO_2$ in the film as identified through XRD analysis. A similar increase in the optical transmission due to the appearance of phase pure $CuCrO_2$ in the films has been reported by Yu et al. [42]. A further increase in the annealing temperature leads to a reduction in the optical transmission values. The observed optical transmission values at a 700 nm wavelength are ~78%, ~71%, and ~62% for the film annealed at 750 °C, 800 °C, and 900 °C, respectively. This is due to the disintegration of the single-phase $CuCrO_2$ and the appearance of Cr and Cr_2O_3 peaks seen in the XRD results. The decreased optical transmission with an increase in the annealing temperature can also be attributed to the increase in the grain sizes, thereby resulting in increased photon scattering [66]. It is evident from the optical transmission data that at a 414 nm wavelength, the transmission spectra of the films annealed at temperatures above 600 °C steeply drops since the films are identified to have a single-phase structure ($CuCrO_2$). However, for the film annealed at 600 °C, the transmission spectra do not drop steeply, which might be possibly due to the two-phase structure (CuO and $CuCr_2O_4$). Similar results have been obtained by Tripathi et al. and Chiba et al. [65,67]. The average optical transmission for the visible wavelength

region obtained at the annealing temperatures of 600 °C, 650 °C, 750 °C, 800 °C, and 900 °C was 40.46%, 61.32%, 57.17%, 54.51%, and 48.57%, respectively.

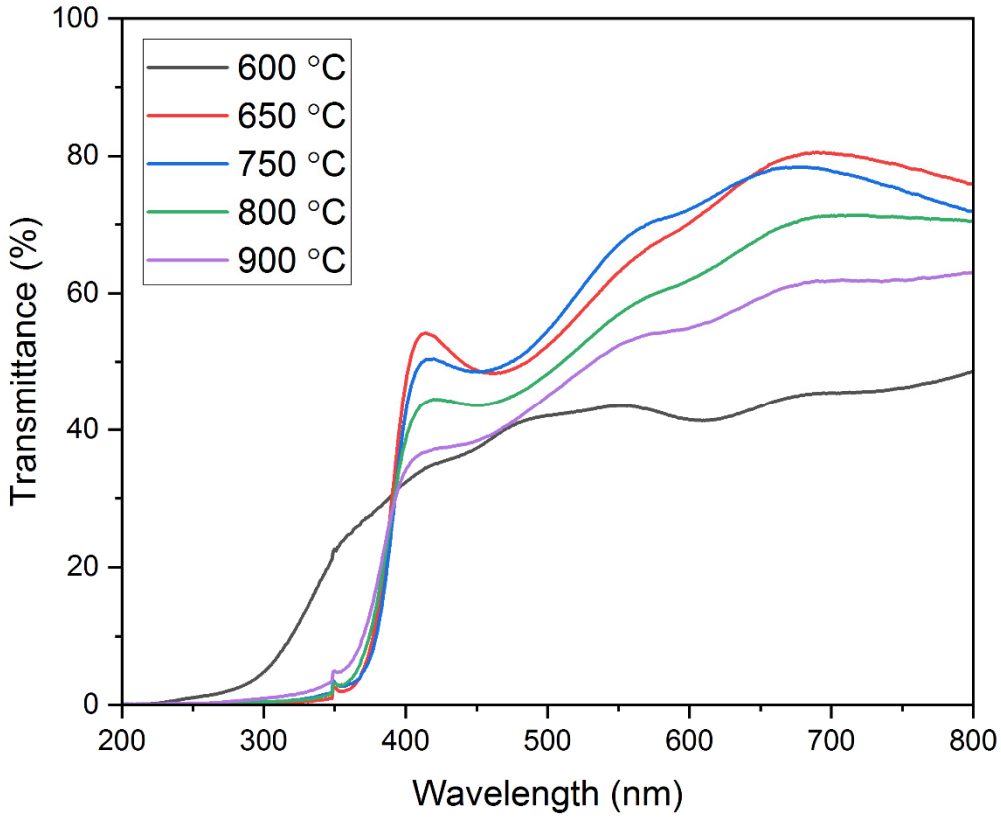

Figure 6. Optical transmission spectra of the films annealed at various annealing temperatures.

Optical Bandgap. The optical bandgap (E_g) of the post-deposition annealed films was calculated using the Tauc plot method [68]. Using the transmission data, the absorption coefficient was calculated using the relation,

$$\alpha = -\frac{2.303}{t} * \log_{10}(\%T) \tag{3}$$

where 't' is the thickness of the thin film post-annealing and '%T' is the fraction of incident light transmitted through the film. The Tauc equation used to calculate the bandgap from the absorption coefficient is,

$$(\alpha h\nu)^{\left(\frac{1}{n}\right)} = B\left(h\nu - E_g\right) \tag{4}$$

where 'hν' is the photon energy and 'n' denotes the nature of the sample's transition. The value of n equals $\frac{1}{2}$, 2, and 3/2 for the direct allowed, indirect allowed, and direct-forbidden transitions, respectively [68–70]. However, the best linear fit of the $(\alpha h\nu)^{(1/n)}$ versus the photon energy curve was obtained for n = $^1/_2$, which allows us to safely conclude that these materials exhibit a direct band gap transition. The resultant Tauc plot thus obtained for the films annealed at various temperatures has been shown in Figure 7.

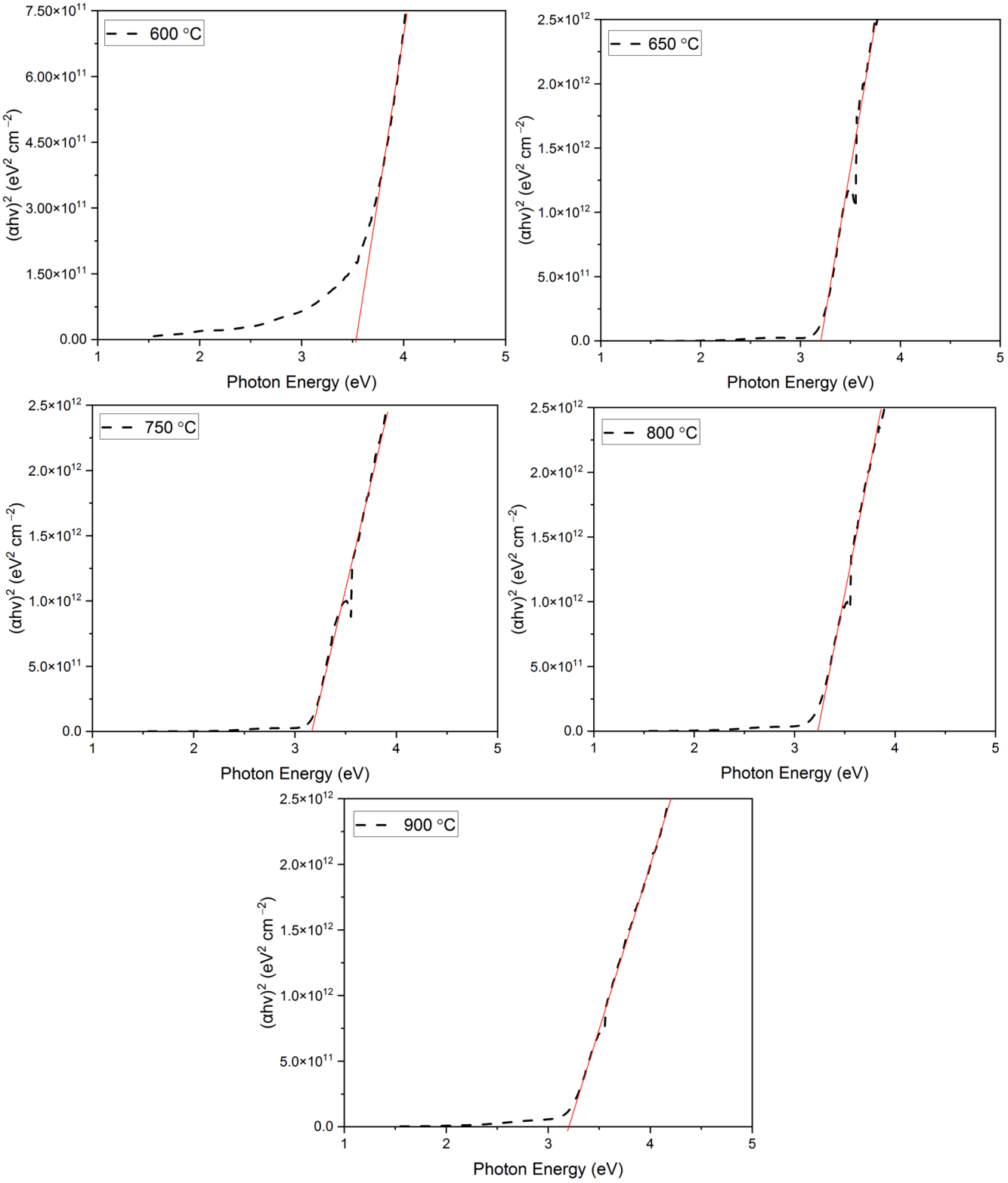

Figure 7. Tauc plot of the films obtained at various annealing temperatures.

The linear portion of the Tauc plot for all the annealed films has been extrapolated to the x-axis to obtain the bandgap values of the films. The obtained bandgap values have been summarized in Table 5.

Table 5. Optical bandgap values of the films obtained at various annealing temperatures.

Annealing Temperature (°C)	Bandgap (eV)
600	3.52
650	3.21
750	3.20
800	3.18
900	3.16

As seen from Table 5, the bandgap values appear to decrease with an increase in the annealing temperature. The bandgap values decreased from 3.52 eV for a 600 °C annealed film to 3.16 for 900 °C. A higher bandgap in a 600 °C annealed film can be attributed to the presence of the CuO phase in the film. Similar bandgap values in CuO-rich films have been reported previously by Vinothkumar et al. [71]. As the annealing temperature is increased, the CuO phase in the film disappears and at the same time, the $CuCrO_2$ phase begins to appear. At 650 °C, a single-phase $CuCrO_2$ thin film is obtained with a bandgap of 3.21 eV, which is close to the previously reported values in the literature [49,65,66,72–75]. With an increase in the annealing temperature, the single-phase $CuCrO_2$ dissociates and exists as two-phase structures. This might be one of the reasons for the increase in the bandgap. This study correlated well with the effect of the annealing temperature study on $CuCrO_2$ thin films conducted by Obulapathi et al. [41].

Electrical Studies. Copper-based delafossites such as $CuCrO_2$, $CuInO_2$, $CuGaO_2$, and $CuFeO_2$ exhibit p-type conductivity due to intrinsic defects such as interstitial oxygen ions and/or Cu vacancies [36]. The p-type conductivity of the $CuCrO_2$ thin films obtained in this research was verified with the help of the hot probe method and a four-point probe. The relation between the annealing temperature and the electrical resistivity of the films is shown in Figure 8. The electrical resistivity was noted to decline from 17.19 Ω cm to 0.652 Ω cm as the annealing temperature was increased from 600 °C to 650 °C. This decrease can be attributed to the appearance of single-phase $CuCrO_2$ in the films. Among all the Cu-based delafossites, $CuCrO_2$ exhibits the lowest resistivity [31]. The previously reported resistivity values for phase pure $CuCrO_2$ are close to the value of 0.652 Ω cm obtained in this research [40,53,76]. With a further increase in the annealing temperature to 750 °C, the resistivity value is seen to increase to 24.67 Ω-cm. This increase in the resistivity is potentially due to the disintegration of single-phase $CuCrO_2$. A sudden increase in the resistivity to 162.7 Ω cm and 351.4 Ω cm is observed at annealing temperatures of 800 °C and 900 °C, respectively. This is likely due to the appearance of Cr_2O_3 phases in the films. Previous literatures have reported the resistivity of Cr_2O_3 to be greater than 1 kΩ cm [77,78]. However, since the films annealed at 800 °C and 900 °C are still $CuCrO_2$ phase-rich, comparatively lower values of resistivity have been observed in this research. It can be safely concluded that the lowest electrical resistivity of 0.652 Ω cm was obtained for films annealed at 650 °C exhibiting single-phase $CuCrO_2$.

Heterojunction Studies. Two configurations of diodes as shown in Figure 9a,b were fabricated to perform the heterojunction studies of $CuCrO_2$ thin films. These diodes will henceforth be called diodes D1 and D2, respectively. For both the diodes, single-phase delafossite $CuCrO_2$ acts as the p-layer and ITO acts as the n-layer. The substrates used for the diodes are 1-20 Ω cm n-type Si. Prior to the deposition of the n and p layers, the Si wafer was dipped in BOE (5:1) for 2 min to remove the native oxide formation. For the heterojunction study, 200 nm thick p-$CuCrO_2$ and 400 nm thick n-ITO layers were used. The deposition parameters used for the n and p layers have been detailed in Tables 1 and 2. The aluminum contact for both diodes have been deposited using the thermal evaporation technique. There are two differences between the two diode configurations. The first difference is the amount of overlap between the two layers. In D1, there is a complete overlap between the two layers. However, the overlap accounts for only 4 mm in the case of D2. The second difference is the way the two diodes are probed during the electrical characterization. D1 has aluminum contacts to be probed on the front and the back of the

Si wafer. On the other hand, D2 has aluminum contacts on the top of the Si wafer. It is necessary to make sure that the current travel is through the p-$CuCrO_2$ and n-ITO layers and not through the Si. For this purpose, dry oxidation using a tube furnace was carried out on the Si wafer used for D2.

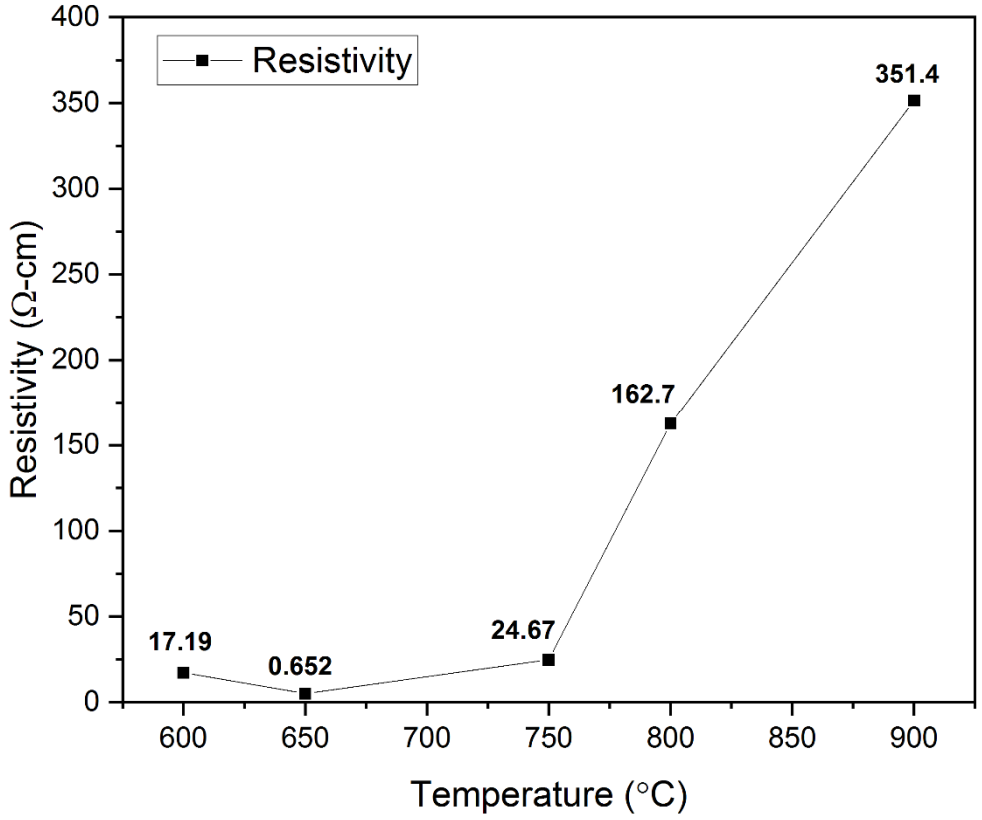

Figure 8. Effect of variation in electrical resistivity with the change in annealing temperature.

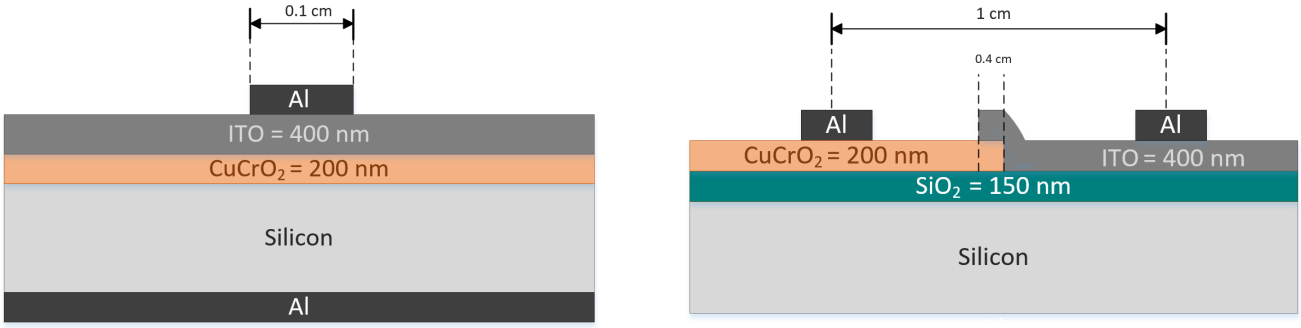

Figure 9. Two configurations of diodes based on p-$CuCrO_2$/n-ITO heterojunction (**a**) D1 and (**b**) D2.

To eliminate the possibility of the formation of a Schottky junction between n-Si and p-$CuCrO_2$, the metal–semiconductor I–V characteristics were analyzed. The contact resistance of the metal–semiconductor junction was determined using the transmission line method (TLM) [79,80]. The contact resistance obtained in this research work is 6.14×10^{-4} Ω-cm^2, which is close to the previously reported value [81]. The I–V characteristics of Si/$CuCrO_2$ shown in Figure 10a indicate a highly linear curve in both a forward and reverse bias. This indicates that the rectification mechanism in D1 and D2 is not due to a Schottky-type rectification. Diodes D1 and D2 show non-linear I–V characteristics as shown in Figure 10b,c. The rectifying behavior of the diodes can be confirmed by the very

low values of the reverse currents. The IV characteristics of the diodes show that there is a higher current flow in D1 as compared to D2. A possible explanation for this can be that looking at the diode's structure, the current travel is purely in the vertical direction for D1. On contrary, in D2, there is a lateral as well as vertical propagation of the current which might lead to the lesser resultant current seen in the I–V characteristics of D2. The calculated diode parameters and their comparison with similar works have been listed in Table 6. The rectification ratio of the diodes has been calculated by taking the ratio of the current for the forward and reverse bias voltages according to Equation (5) [82,83],

$$Rectification\ Ratio = \frac{I_{ON}}{I_{OFF}} \tag{5}$$

On comparing the rectification performance of the two diodes, it was noticed that D1 has a lower turn-on voltage of 0.85 V as compared to 1.29 V for D2. Further, the rectification ratio of D1 is 2375, which is substantially greater than the rectification ratio of 1664 for D2. The rectification ratio of D1 is two orders of magnitude greater compared to the reported values on the diodes prepared with $CuCrO_2$ as the p-layer [83]. The rectification ratios indicate that D1 must have a lower leakage current as compared to D2, which is evident in the results. D1 has a leakage current of the order of 1.24×10^{-8} A and that of D2 is of the order of 2.15×10^{-8} A. The Ln (current density (J)) versus the voltage for both diodes have been shown in Figure 10d,e. It can be seen from the current density plot that the rectification for the forward bias voltages is much larger in the case of D1. From the electrical characterization of the two diodes, it is safe to say that a superior device performance is obtained for D1 compared to D2.

The ideality factor of the diode is used to measure the performance of the diode in comparison to the ideal diode. The ideality factor can be calculated using the diode equation [84],

$$I = I_o\left(e^{\frac{qV}{nkT}} - 1\right) \tag{6}$$

$$n = \frac{q}{kT}.\frac{dV}{d(LnJ)} \tag{7}$$

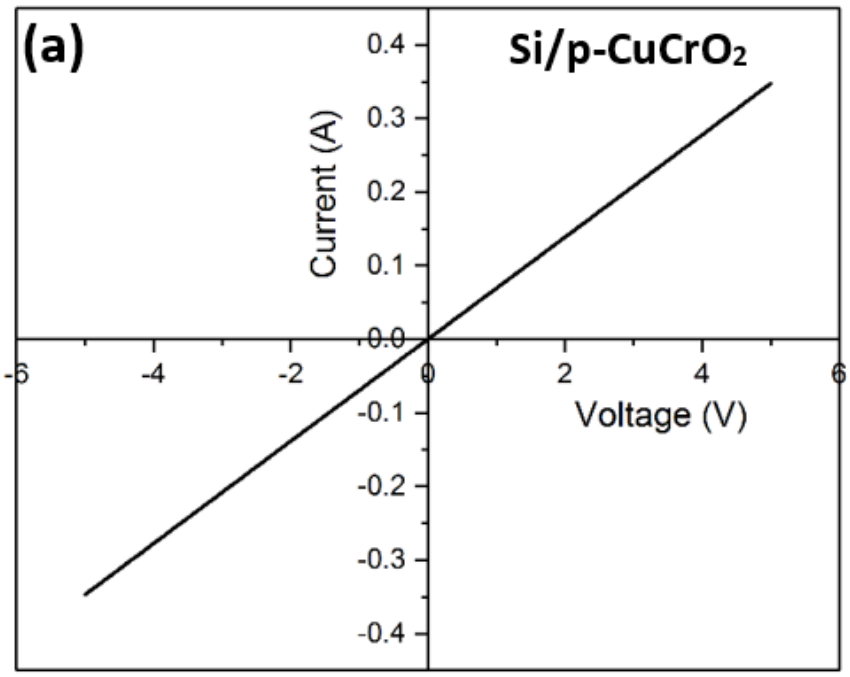

Figure 10. *Cont.*

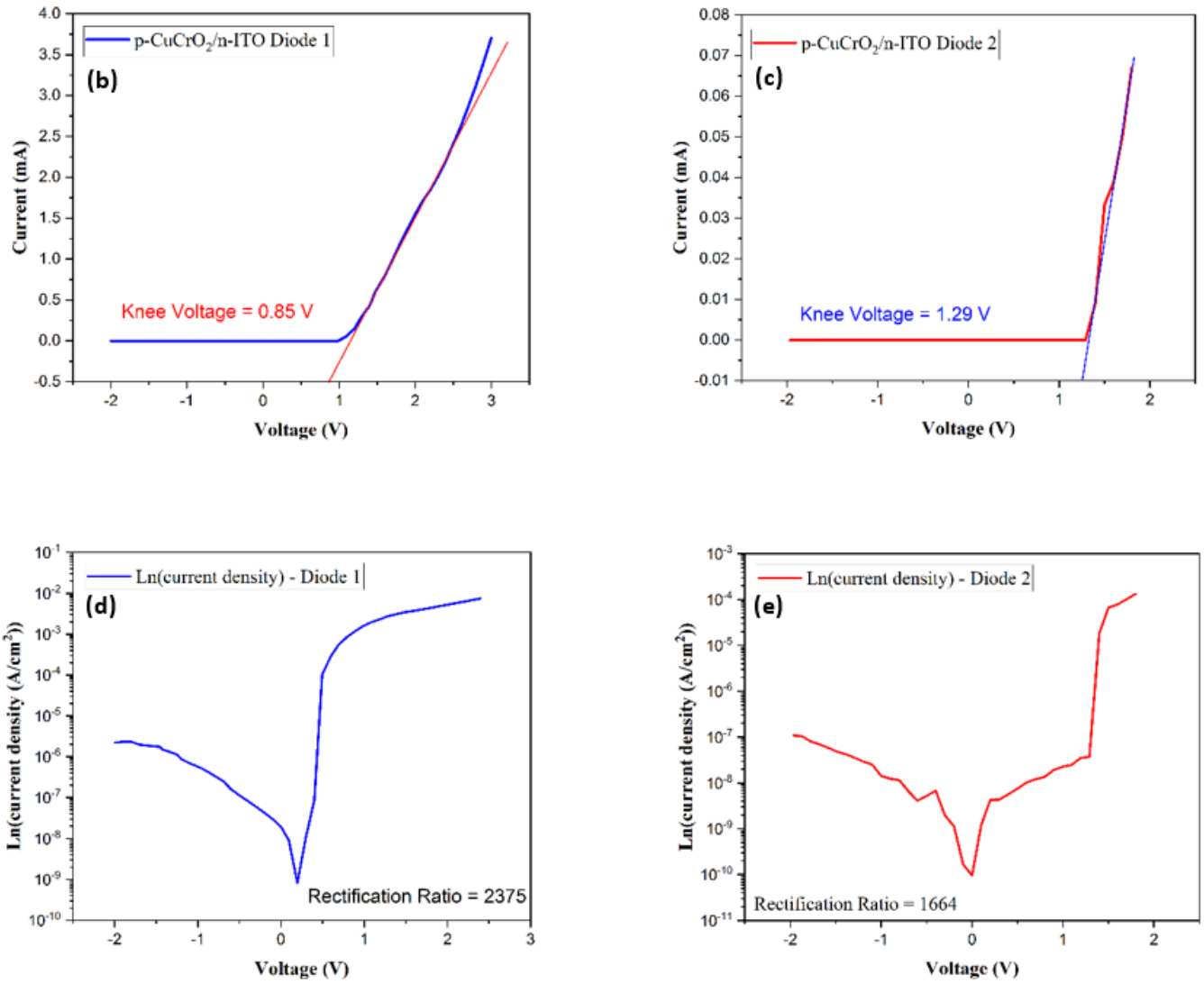

Figure 10. (**a**) I–V characteristics of Si/p-$CuCrO_2$, (**b**) I–V characteristics of D1, (**c**) I–V characteristics of D2, (**d**) Ln (current density) vs. voltage of D1, and (**e**) Ln (current density) vs. voltage of D2.

The diode ideality factor was thus determined by calculating the slope of Ln (current density) versus the voltage graphs shown in Figure 10d,e. The diode D1 exhibits an ideality factor of 4.13 while the ideality factor of the diode D2 was obtained as 5.8. In the case of an ideal pn-junction diode, the ideality factor is 1, where the conduction of the electrons due to thermionic diffusion is acting. The rise in the ideality factor observed in this research work can be attributed to the use of compounds as layers forming the diode, the recombination of carriers, the conduction of electrons by tunneling from the active layer to the p-region acting as the barrier layer, etc. [84–86]. It is also observed that lattice matching plays an important role in the rectification ratio and the ideality factor of the diode. For homojunction diodes, the ideality factor is noticed to be below two, whereas the ideality factor rises above two for a heterojunction diode [84,87–90].

To study the optical transparency of D1, the p-$CuCrO_2$/n-ITO stack without the Al layers was deposited on a cleaned quartz substrate. The transparency of D1 can be verified through the optical study results shown in Figure 11a–c. It is evident that the p-$CuCrO_2$/n-ITO stack has greater than 60% transmission for the wavelengths of light greater than 550 nm. The optical bandgap of the stack was calculated from the Tauc plot and was obtained as 3.25 eV. Figure 11c clearly shows the photomicrograph of the p-$CuCrO_2$/n-ITO stack deposited on the quartz substrate through which the details written on the paper can be

clearly read. The results obtained through the heterojunction study confirmed that the diode D1 with a complete overlap between the semiconducting layers showed a superior performance over the diode D2, which had an overlap of only 4 mm.

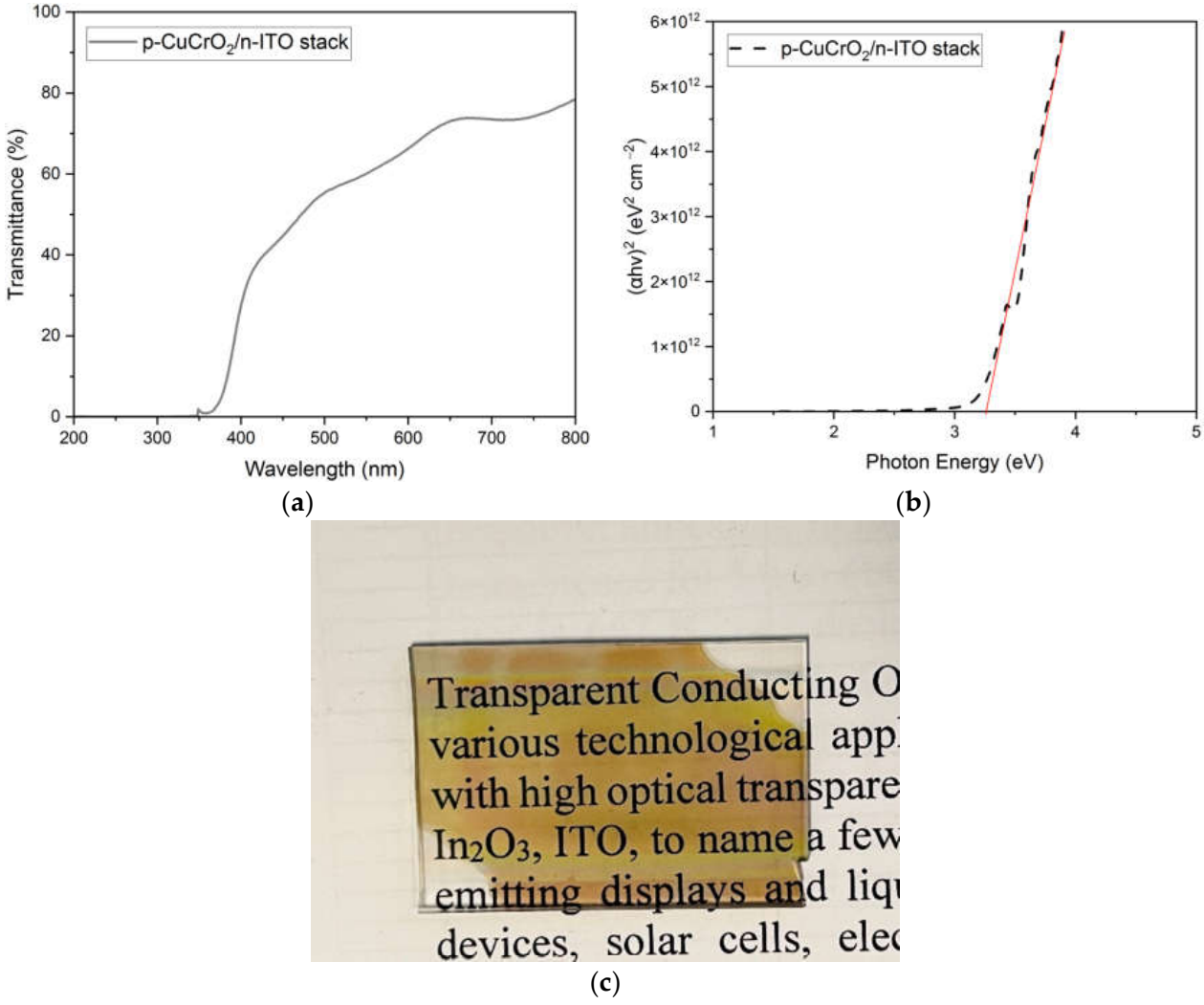

Figure 11. Results of the optical study conducted on p-$CuCrO_2$/n-ITO stack deposited on a quartz substrate. (**a**) Optical transmission of the stack, (**b**) Tauc plot of the stack, and (**c**) photomicrograph of the stack showing high transparency.

Table 6. Electrical characterization results of D1 and D2 and comparison with similar works.

Diode	Turn ON Voltage (V)	Leakage Current (A)	Rectification Ratio	Ideality Factor	Reference
D1	0.85	1.24×10^{-8} (at 0.9 V)	2375 (at 2 V)	4.13	This work
D2	1.29	2.15×10^{-8} (at 0.9 V)	1664 (at 1.8 V)	5.8	This work
n-ITO/p-$CuCrO_2$	~0.87	NR	$>10^4$	3.90	[49]
n-ZnO/p-$Cu_{0.66}Cr_{1.33}O_2$	1.40	NR	13	6.30	[90]
n-ZnO/p-Mg:$CuCrO_2$	~2.00	NR	~7–10	NR	[91]
n-ZnO/p-$CuCrO_2$	NR	NR	107	1.56	[92]
n-ZnO/p-$CuCrO_2$	NR	NR	20	2.20	[93]

4. Conclusions

For the first time, p-type delafossite phase $CuCrO_2$ thin films were deposited using the dual target RF magnetron sputtering of Cu_2O and Cr_2O_3 targets, followed by an annealing treatment. Through this work, it was established that the annealing temperature plays a critical role in controlling the electrical, optical, structural, and morphological properties of the film. Using XRD analysis, it was confirmed that the single-phase delafossite structure of $CuCrO_2$ thin films was obtained at 650 °C of the annealing temperature. Annealing at a lower or higher temperature from 650 °C leads to the formation of two-phase structures. The XPS analysis confirmed the presence of Cr in the 3+ oxidation state and Cu in the 1+ oxidation state through the absence of satellite peaks in the Cu core level XPS spectrum and the appearance of a Cu LMM Auger peak in the Cr core level XPS spectrum. The XPS results further asserted the successful synthesis of phase pure $CuCrO_2$ thin films at an annealing temperature of 650 °C. Nanocrystalline growth was observed in all the films studied in this research through FESEM images. The images also confirmed the increasing trend of the average grain size from 40.22 nm to 105.31 nm as the annealing temperature increased from 600 °C to 900 °C. The optical studies revealed that the highest transmission of ~81% and an optical bandgap of 3.21 eV was obtained for the films annealed at 650 °C. The bandgap values were found to vary between 3.52 eV and 3.16 eV as the annealing temperature increased. The lowest resistivity value of 0.652 Ω cm was obtained for the film showing the single-phase $CuCrO_2$ delafossite structure. This low resistivity value permitted its use for the study of the transparent heterojunction study in this research. Two highly transparent heterojunctions comprising p-$CuCrO_2$ and n-ITO layers were fabricated. It was found that the diode D1 with a complete overlap between the semiconducting layers showed a superior performance over the diode D2, which had an overlap of only 4 mm. The leakage current and the knee voltage of the diode D1 were identified as 2.15×10^{-8} A and 0.85 V, respectively. The forward-to-reverse current rectification ratio of the diode D1 was calculated to be 2375, which is much higher than the previously reported values. The ideality factor of the diode D1 was calculated to be 4.13. The p-$CuCrO_2$/n-ITO stack was deposited on quartz for optical studies, revealing a high optical transmission of greater than 60% at wavelengths greater than 550 nm and an optical bandgap of 3.25 eV. The results reported in this research work make the phase pure delafossite structure of $CuCrO_2$ an ideal candidate for transparent electronics applications.

Author Contributions: Conceptualization, S.S. and K.B.S.; methodology, S.S.; validation, S.S. and K.B.S.; investigation, S.S.; data curation, S.S., A.H.B.; writing-original draft preparation, S.S.; writing-review and editing, S.S., A.H.B., K.B.S.; visualization, S.S.; supervision, K.B.S. All authors have read and agreed to the published version of the manuscript.

Funding: The APC was funded by The College of Graduate Studies, University of Central Florida, Orlando, FL 32816.

Institutional Review Board Statement: Not applicable.

Informed Consent Statement: Not applicable.

Data Availability Statement: Not applicable.

Acknowledgments: The authors would like to acknowledge the NSF MRI: ECCS: 1726636 and MCF-AMPAC facility, MSE, and CECS for the XPS use.

Conflicts of Interest: The authors declare no conflict of interest.

References

1. Hu, L.; Wei, R.H.; Tang, X.W.; Lu, W.J.; Zhu, X.B.; Sun, Y.P. Design strategy for p-type transparent conducting oxides. *J. Appl. Phys.* **2020**, *128*, 140902. [CrossRef]
2. Stadler, A. Transparent Conducting Oxides—An Up-To-Date Overview. *Materials* **2012**, *5*, 661–683. [CrossRef] [PubMed]
3. Robertson, J.; Peacock, P.W.; Towler, M.D.; Needs, R. Electronic structure of p-type conducting transparent oxides. *Thin Solid Films* **2002**, *411*, 96–100. [CrossRef]

4. Afre, R.A.; Sharma, N.; Sharon, M.; Sharon, M. Transparent Conducting Oxide Films for Various Applications: A Review. *Rev. Adv. Mater. Sci.* **2018**, *53*, 79–89. [CrossRef]
5. Lan, J.-H.; Kanicki, J.; Catalano, A.; Keane, J.; Boer, W.D.; Gu, T. Patterning of transparent conducting oxide thin films by wet etching for a-Si:H TFT-LCDs. *J. Electron. Mater.* **1996**, *25*, 1806–1817. [CrossRef]
6. Afzal, A.M.; Dastgeer, G.; Iqbal, M.Z.; Gautam, P.; Faisal, M.M. High-Performance p-BP/n-PdSe2 Near-Infrared Photodiodes with a Fast and Gate-Tunable Photoresponse. *ACS Appl. Mater. Interfaces* **2020**, *12*, 19625–19634. [CrossRef] [PubMed]
7. Orak, İ.; Ejderha, K.; Sönmez, E.; Alanyalıoğlu, M.; Turut, A. The effect of annealing temperature on the electrical characterization of Co/n type GaP Schottky diode. *Mater. Res. Bull.* **2015**, *61*, 463–468. [CrossRef]
8. Kudo, A.; Yanagi, H.; Ueda, K.; Hosono, H.; Kawazoe, H.; Yano, Y. Fabrication of transparent p–n heterojunction thin film diodes based entirely on oxide semiconductors. *Appl. Phys. Lett.* **1999**, *75*, 2851–2853. [CrossRef]
9. Bright, C.I. Chapter 21—Transparent conductive thin films. In *Optical Thin Films and Coatings*, 2nd ed.; Piegari, A., Flory, F., Eds.; Woodhead Publishing: Cambridge, UK, 2018; pp. 741–788.
10. Sundaresh, S.; Nehate, S.D.; Sundaram, K.B. Electrical and Optical Studies of Reactively Sputtered Indium Oxide Thin Films. *ECS J. Solid State Sci. Technol.* **2021**, *10*, 065016. [CrossRef]
11. Sundaresh, S.; Nehate, S.D.; Sundaram, K.B. Investigation of Electrical and Optical Properties of Low Resistivity Indium Oxide Thin Films. *ECS Trans.* **2021**, *102*, 95–111. [CrossRef]
12. Xu, J.; Liu, J.-B.; Liu, B.-X.; Li, S.-N.; Wei, S.-H.; Huang, B. Design of n-Type Transparent Conducting Oxides: The Case of Transition Metal Doping in In_2O_3. *Adv. Electron. Mater.* **2018**, *4*, 1700553. [CrossRef]
13. George, J.; Menon, C.S. Electrical and optical properties of electron beam evaporated ITO thin films. *Surf. Coat. Technol.* **2000**, *132*, 45–48. [CrossRef]
14. Fallah, H.R.; Ghasemi, M.; Hassanzadeh, A.; Steki, H. The effect of annealing on structural, electrical and optical properties of nanostructured ITO films prepared by e-beam evaporation. *Mater. Res. Bull.* **2007**, *42*, 487–496. [CrossRef]
15. Samadi, M.; Zirak, M.; Naseri, A.; Khorashadizade, E.; Moshfegh, A.Z. Recent progress on doped ZnO nanostructures for visible-light photocatalysis. *Thin Solid Films* **2016**, *605*, 2–19. [CrossRef]
16. Dixon, S.C.; Sathasivam, S.; Williamson, B.A.D.; Scanlon, D.O.; Carmalt, C.J.; Parkin, I.P. Transparent conducting n-type ZnO:Sc—Synthesis, optoelectronic properties and theoretical insight. *J. Mater. Chem. C* **2017**, *5*, 7585–7597. [CrossRef]
17. Cheng, D.; Zhang, M.; Chen, J.; Yang, C.; Zeng, X.; Cao, D. Computer Screening of Dopants for the Development of New SnO_2-Based Transparent Conducting Oxides. *J. Phys. Chem. C* **2014**, *118*, 2037–2043. [CrossRef]
18. Terrier, C.; Chatelon, J.P.; Roger, J.A. Electrical and optical properties of Sb:SnO_2 thin films obtained by the sol-gel method. *Thin Solid Films* **1997**, *295*, 95–100. [CrossRef]
19. Jiménez-González, A.E.; Soto Urueta, J.A.; Suárez-Parra, R. Optical and electrical characteristics of aluminum-doped ZnO thin films prepared by solgel technique. *J. Cryst. Growth* **1998**, *192*, 430–438. [CrossRef]
20. Shan, F.K.; Yu, Y.S. Band gap energy of pure and Al-doped ZnO thin films. *J. Eur. Ceram. Soc.* **2004**, *24*, 1869–1872. [CrossRef]
21. Maldonado, F.; Stashans, A. Al-doped ZnO: Electronic, electrical and structural properties. *J. Phys. Chem. Solids* **2010**, *71*, 784–787. [CrossRef]
22. Shantheyanda, B.; Sundaram, K.B.; Shiradkar, N. Studies on the effect of hydrogen doping during deposition of Al:ZnO films using RF magnetron sputtering. *Mater. Sci. Eng. B* **2012**, *177*, 1777–1782. [CrossRef]
23. Shantheyanda, B.P.; Todi, V.; Sundaram, K.B.; Vijayakumar, A.; Oladeji, I.O. Compositional study of vacuum annealed Al doped ZnO thin films obtained by RF magnetron sputtering. *J. Vac. Sci. Technol.* **2011**, *29*, 051514. [CrossRef]
24. Mariappan, R.; Ponnuswamy, V.; Suresh, P.; Suresh, R.; Ragavendar, M.; Sankar, C. Deposition and characterization of pure and Cd doped SnO_2 thin films by the nebulizer spray pyrolysis (NSP) technique. *Mater. Sci. Semicond. Process.* **2013**, *16*, 825–832. [CrossRef]
25. de Moure-Flores, F.; Quiñones-Galván, J.G.; Hernández-Hernández, A.; Guillén-Cervantes, A.; Santana-Aranda, M.A.; Olvera, M.D.L.L.; Meléndez-Lira, M. Structural, optical and electrical properties of Cd-doped SnO_2 thin films grown by RF reactive magnetron co-sputtering. *Appl. Surf. Sci.* **2012**, *258*, 2459–2463. [CrossRef]
26. Senthilkumar, P.; Vasuki, G.; Babu, R.R.; Raja, S. Influence of Cd doping on the structural, optical and morphological properties of SnO_2 thin films. *AIP Conf. Proc.* **2020**, *2220*, 090024.
27. Kawazoe, H.; Yasukawa, M.; Hyodo, H.; Kurita, M.; Yanagi, H.; Hosono, H. P-type electrical conduction in transparent thin films of $CuAlO_2$. *Nature* **1997**, *389*, 939–942. [CrossRef]
28. Hautier, G.; Miglio, A.; Ceder, G.; Rignanese, G.-M.; Gonze, X. Identification and design principles of low hole effective mass p-type transparent conducting oxides. *Nat. Commun.* **2013**, *4*, 2292. [CrossRef]
29. Banerjee, A.N.; Chattopadhyay, K.K. Recent developments in the emerging field of crystalline p-type transparent conducting oxide thin films. *Prog. Cryst. Growth Charact. Mater.* **2005**, *50*, 52–105. [CrossRef]
30. Zhang, K.H.L.; Xi, K.; Blamire, M.G.; Egdell, R.G. P-type transparent conducting oxides. *J. Phys. Condens. Matter* **2016**, *28*, 383002. [CrossRef]
31. Moreira, M.; Afonso, J.; Crepelliere, J.; Lenoble, D.; Lunca-Popa, P. A review on the p-type transparent Cu–Cr–O delafossite materials. *J. Mater. Sci.* **2022**, *57*, 3114–3142. [CrossRef]
32. Nagarajan, R.; Duan, N.; Jayaraj, M.K.; Li, J.; Vanaja, K.A.; Yokochi, A.; Draeseke, A.; Tate, J.; Sleight, A.W. p-Type conductivity in the delafossite structure. *Int. J. Inorg. Mater.* **2001**, *3*, 265–270. [CrossRef]

33. Iozzi, M.F.; Vajeeston, P.; Vidya, R.; Ravindran, P.; Fjellvåg, H. Structural and electronic properties of transparent conducting delafossite: A comparison between the $AgBO_2$ and $CuBO_2$ families (B = Al, Ga, In and Sc, Y). *RSC Adv.* **2015**, *5*, 1366–1377. [CrossRef]
34. Yu, R.-S.; Lee, Y.-C. Effects of annealing on the optical and electrical properties of sputter-deposited $CuGaO_2$ thin films. *Thin Solid Films* **2018**, *646*, 143–149. [CrossRef]
35. Saikumar, A.K.; Sundaresh, S.; Nehate, S.D.; Sundaram, K.B. Preparation and Characterization of Radio Frequency Sputtered Delafossite p-type Copper Gallium Oxide (p-$CuGaO_2$) Thin Films. *ECS J. Solid State Sci. Technol.* **2022**, *11*, 023005. [CrossRef]
36. Saikumar, A.K.; Sundaresh, S.; Sundaram, K.B. Preparation and Characterization of p-Type Copper Gallium Oxide ($CuGaO_2$) Thin Films by Dual Sputtering Using Cu and Ga_2O_3 Targets. *ECS J. Solid State Sci. Technol.* **2022**, *11*, 065010. [CrossRef]
37. Ehara, T. Preparation of $CuGaO_2$ Thin Film by a Sol-Gel Method Using Two Kinds of Metal Source Combination. *J. Mater. Sci. Chem. Eng.* **2018**, *6*, 68–78.
38. Zhang, N.; Sun, J.; Gong, H. Transparent p-Type Semiconductors: Copper-Based Oxides and Oxychalcogenides. *Coatings* **2019**, *9*, 137. [CrossRef]
39. Bai, Z.; Chen, S.-C.; Lin, S.-S.; Shi, Q.; Lu, Y.-B.; Song, S.-M.; Sun, H. Review in optoelectronic properties of p-type $CuCrO_2$ transparent conductive films. *Surf. Interfaces* **2021**, *22*, 100824. [CrossRef]
40. Chiba, H.; Hosaka, N.; Kawashima, T.; Washio, K. Thermal solid-phase crystallization of amorphous $CuCrO_2$:N thin films deposited by reactive radio-frequency magnetron sputtering. *Thin Solid Films* **2018**, *652*, 16–22. [CrossRef]
41. Obulapathi, L. Effect of Annealing Temperature on Structural, Electrical and Optical Properties of $CuCrO_2$ Thin Films by Reactive dc Magnetron Sputtering. *Indian J. Pure Appl. Phys.* **2014**, *4*, 16–19. Available online: http://www.urpjournals.com:16-19 (accessed on 25 December 2022).
42. Yu, R.-S.; Tasi, C.-P. Structure, composition and properties of p-type $CuCrO_2$ thin films. *Ceram. Int.* **2014**, *40*, 8211–8217. [CrossRef]
43. Ahmadi, M.; Asemi, M.; Ghanaatshoar, M. Improving the electrical and optical properties of $CuCrO_2$ thin film deposited by reactive RF magnetron sputtering in controlled N_2/Ar atmosphere. *Appl. Phys. A* **2018**, *124*, 529. [CrossRef]
44. Yu, R.-S.; Hu, D.-H. Formation and characterization of p-type semiconductor $CuCrO_2$ thin films prepared by a sol-gel method. *Ceram. Int.* **2015**, *41*, 9383–9391. [CrossRef]
45. Yu, R.-S.; Wu, C.-M. Characteristics of p-type transparent conductive $CuCrO_2$ thin films. *Appl. Surf. Sci.* **2013**, *282*, 92–97. [CrossRef]
46. Chiu, T.-W.; Yang, Y.-C.; Yeh, A.-C.; Wang, Y.-P.; Feng, Y.-W. Antibacterial property of $CuCrO_2$ thin films prepared by RF magnetron sputtering deposition. *Vacuum* **2013**, *87*, 174–177. [CrossRef]
47. Li, J.-P.; O'Neil, H.S.C.; Seifert, F. Subsolidus Phase Relations in the System MgO—SiO_2—Gr—O in Equilibrium with Metallic Cr, and their Significance for the Petrochemistry of Chromium. *J. Petrol.* **1995**, *36*, 107–132. [CrossRef]
48. Novikov, V.; Xanthopoulou, G.; Knysh, Y.; Amosov, A.P. Solution Combustion Synthesis of nanoscale Cu-Cr-O spinels: Mechanism, properties and catalytic activity in CO oxidation. *Ceram. Int.* **2017**, *43*, 11733–11742. [CrossRef]
49. Bottiglieri, L. Out of Stoichiometry $CuCrO_2$ as Transparent p-Type Semiconductor for Photovoltaics and Transparent Electronics. Ph.D. Thesis, Université Grenoble Alpes, Grenoble, France, 2022.
50. Schorne-Pinto, J.; Chartrand, P.; Barnabé, A.; Cassayre, L. Thermodynamic and Structural Properties of $CuCrO_2$ and $CuCr_2O_4$: Experimental Investigation and Phase Equilibria Modeling of the Cu–Cr–O System. *J. Phys. Chem. C* **2021**, *125*, 15069–15084. [CrossRef]
51. Chen, H.-Y.; Chang, K.-P. Influence of Post-Annealing Conditions on the Formation of Delafossite-$CuCrO_2$ Films. *ECS J. Solid State Sci. Technol.* **2013**, *2*, P76. [CrossRef]
52. Chen, H.-Y.; Yang, W.-J.; Chang, K.-P. Characterization of delafossite-$CuCrO_2$ thin films prepared by post-annealing using an atmospheric pressure plasma torch. *Appl. Surf. Sci.* **2012**, *258*, 8775–8779. [CrossRef]
53. Wu, S.; Deng, Z.; Dong, W.; Shao, J.; Fang, X. Effect of deposition atmosphere on the structure and properties of Mg doped $CuCrO_2$ thin films prepared by direct current magnetron sputtering. *Thin Solid Films* **2015**, *595*, 124–128. [CrossRef]
54. Crêpellière, J.; Popa, P.L.; Bahlawane, N.; Leturcq, R.; Werner, F.; Siebentritt, S.; Lenoble, D. Transparent conductive $CuCrO_2$ thin films deposited by pulsed injection metal organic chemical vapor deposition: Up-scalable process technology for an improved transparency/conductivity trade-off. *J. Mater. Chem. C* **2016**, *4*, 4278–4287. [CrossRef]
55. Le, T.K.; Flahaut, D.; Martinez, H.; Andreu, N.; Gonbeau, D.; Pachoud, E.; Pelloquin, D.; Maignan, A. The electronic structure of the $CuRh_{1-x}Mg_xO_2$ thermoelectric materials: An X-ray photoelectron spectroscopy study. *J. Solid State Chem.* **2011**, *184*, 2387–2392. [CrossRef]
56. Briggs, D. *Handbook of X-ray Photoelectron Spectroscopy*; Wanger, C., Riggs, W., Davis, L., Moulder, J., Muilenberg, G.E., Eds.; Perkin-Elmer Corp.: Eden Prairie, MN, USA, 1979; p. 190.
57. Sundaresh, S.; Saikumar, A.K.; Sundaram, K.B. Investigation on the Intermixing of Cu and In Layers for the Formation of $Cu_2In_2O_5$ Thin Films. *ECS J. Solid State Sci. Technol.* **2022**, *11*, 085003. [CrossRef]
58. Bottiglieri, L.; Resende, J.; Weber, M.; Chaix-Pluchery, O.; Jiménez, C.; Deschanvres, J.-L. Out of stoichiometry $CuCrO_2$ films as a promising p-type TCO for transparent electronics. *Mater. Adv.* **2021**, *2*, 4721–4732. [CrossRef]
59. Lin, F.; Gao, C.; Zhou, X.; Shi, W.; Liu, A. Magnetic, electrical and optical properties of p-type Fe-doped $CuCrO_2$ semiconductor thin films. *J. Alloys Compd.* **2013**, *581*, 502–507. [CrossRef]

60. Kim, J.; Kendall, O.; Ren, J.; Murdoch, B.J.; McConville, C.F.; van Embden, J.; Della Gaspera, E. Highly Conductive and Visibly Transparent p-Type $CuCrO_2$ Films by Ultrasonic Spray Pyrolysis. *ACS Appl. Mater. Interfaces* **2022**, *14*, 11768–11778. [CrossRef]
61. Wang, J.; Zheng, P.; Zhou, X.; Liang, F. Investigation of structural, morphological, optical, and electrical properties of $CuCrO_2$ films prepared by sol-gel method. *J. Sol-Gel Sci. Technol.* **2016**, *79*, 37–43. [CrossRef]
62. Abdullah, M.M.; Rajab, F.M.; Al-Abbas, S.M. Structural and optical characterization of Cr_2O_3 nanostructures: Evaluation of its dielectric properties. *AIP Adv.* **2014**, *4*, 027121. [CrossRef]
63. Gandhi, A.A.-O.; Li, T.Y.; Chan, T.S.; Wu, S.A.-O. Short-Range Correlated Magnetic Core-Shell CrO_2/Cr_2O_3 Nanorods: Experimental Observations and Theoretical Considerations. *Nanomaterials* **2018**, *8*, 312. [CrossRef]
64. Lin, S.S.; Shi, Q.; Dai, M.J.; Wang, K.L.; Chen, S.C.; Kuo, T.Y.; Liu, D.G.; Song, S.M.; Sun, H. The Optoelectronic Properties of p-Type Cr-Deficient $Cu[Cr_{0.95-x}Mg_{0.05}]O_2$ Films Deposited by Reactive Magnetron Sputtering. *Materials* **2020**, *13*, 2376. [CrossRef] [PubMed]
65. Tripathi, T.S.; Karppinen, M. Structural Optical and Electrical Transport Properties of ALD-Fabricated $CuCrO_2$ Films. *Phys. Procedia* **2015**, *75*, 488–494. [CrossRef]
66. Sánchez-Alarcón, R.I.; Oropeza-Rosario, G.; Gutierrez-Villalobos, A.; Muro-López, M.A.; Martínez-Martínez, R.; Zaleta-Alejandre, E.; Falcony, C.; Alarcón-Flores, G.; Fragoso, R.; Hernández-Silva, O.; et al. Ultrasonic spray-pyrolyzed $CuCrO_2$ thin films. *J. Phys. D Appl. Phys.* **2016**, *49*, 175102. [CrossRef]
67. Chiba, H.; Kawashima, T.; Washio, K. Optical and structural properties of $CuCrO_2$ thin films on c-face sapphire substrate deposited by reactive RF magnetron sputtering. *Mater. Sci. Semicond. Process.* **2017**, *70*, 234–238. [CrossRef]
68. Tauc, J.; Grigorovici, R.; Vancu, A. Optical Properties and Electronic Structure of Amorphous Germanium. *Phys. Status Solidi B* **1966**, *15*, 627–637. [CrossRef]
69. Abeles, F. *Optical Properties of Solids*; North-Holland Pub. Co.: Amsterdam, The Netherlands; American Elsevier: New York, NY, USA, 1972.
70. Davis, E.A.; Mott, N.F. Conduction in non-crystalline systems V. Conductivity, optical absorption and photoconductivity in amorphous semiconductors. *Philos. Mag.* **1970**, *22*, 0903–0922. [CrossRef]
71. Vinothkumar, P.; Manoharan, C.; Shanmugapriya, B.; Bououdina, M. Effect of reaction time on structural, morphological, optical and photocatalytic properties of copper oxide (CuO) nanostructures. *J. Mater. Sci. Mater. Electron.* **2019**, *30*, 6249–6262. [CrossRef]
72. Moreno-Camacho, C.A.; Montoya-Torres, J.R.; Jaegler, A.; Gondran, N. Sustainability metrics for real case applications of the supply chain network design problem: A systematic literature review. *J. Clean. Prod.* **2019**, *231*, 600–618. [CrossRef]
73. Zhou, X.; Lin, F.; Shi, W.; Liu, A. Structural, electrical, optical and magnetic properties of p-type $Cu(Cr_{1-x}Mn_x)O_2$ thin films prepared by pulsed laser deposition. *J. Alloys Compd.* **2014**, *614*, 221–225. [CrossRef]
74. Chen, H.-Y.; Chang, K.-P.; Yang, C.-C. Characterization of transparent conductive delafossite-$CuCr_{1-x}O_2$ films. *Appl. Surf. Sci.* **2013**, *273*, 324–329. [CrossRef]
75. Shin, D.; Foord, J.S.; Egdell, R.G.; Walsh, A. Electronic structure of $CuCrO_2$ thin films grown on $Al_2O_3(001)$ by oxygen plasma assisted molecular beam epitaxy. *J. Appl. Phys.* **2012**, *112*, 113718. [CrossRef]
76. Jantrasee, S.; Ruttanapun, C. Impact of Sn^{4+} Substitution at Cr^{3+} Sites on Thermoelectric and Electronic Properties of p-Type Delafossite $CuCrO_2$. *J. Electron. Mater.* **2020**, *49*, 601–610. [CrossRef]
77. Singh, J.; Verma, V.; Kumar, R.; Kumar, R. Structural, optical and electrical characterization of epitaxial Cr_2O_3 thin film deposited by PLD. *Mater. Res. Express* **2019**, *6*, 106406. [CrossRef]
78. Cheng, C.-S.; Gomi, H.; Sakata, H. Electrical and Optical Properties of Cr_2O_3 Films Prepared by Chemical Vapour Deposition. *Phys. Status Solidi A* **1996**, *155*, 417–425. [CrossRef]
79. Reeves, G.K.; Harrison, H.B. Obtaining the specific contact resistance from transmission line model measurements. *IEEE Electron Device Lett.* **1982**, *3*, 111–113. [CrossRef]
80. Cohen, S.S. Contact Resistance and Methods for its Determination. *MRS Proc.* **1982**, *18*, 361. [CrossRef]
81. Lim, W.T.; Stafford, L.; Sadik, P.W.; Norton, D.P.; Pearton, S.J.; Wang, Y.L.; Ren, F. Ni/Au Ohmic contacts to p-type Mg-doped $CuCrO_2$ epitaxial layers. *Appl. Phys. Lett.* **2007**, *90*, 142101. [CrossRef]
82. Sherif, S.; Rubio-Bollinger, G.; Fau-Pinilla-Cienfuegos, E.; Pinilla-Cienfuegos, E.; Fau-Coronado, E.; Coronado, E.; Fau-Cuevas, J.C.; Cuevas, J.C.; Fau-Agraït, N.; Agraït, N. Current rectification in a single molecule diode: The role of electrode coupling. *Nanotechnology* **2015**, *26*, 291001. [CrossRef]
83. Bottiglieri, L.; Sekkat, A.; Belmouhoub, M.; Resende, J.; Nguyen, V.H.; Weber, M.; Munoz Rojas, D.; Jiménez, C.; Deschanvres, J.-L. n-ZnO/Out-of-Stoichiometry p-$CuCrO_2$ Diodes for Efficient and Low-Cost Transparent Electronic Applications. *ACS Appl. Electron. Mater.* **2022**, *4*, 5847–5858. [CrossRef]
84. Rahman, H.; Esthan, C.; Nair, B.G.; Sreeram, P.R.; Shinoj, V.K.; Behera, P.; Deshpande, U.; Philip, R.R. Band structure and diode characteristics of transparent pn-homojunction using delafossite $CuInO_2$. *J. Phys. D Appl. Phys.* **2020**, *53*, 015102. [CrossRef]
85. Sah, C.T.; Noyce, R.N.; Shockley, W. Carrier Generation and Recombination in P-N Junctions and P-N Junction Characteristics. *Proc. IRE* **1957**, *45*, 1228–1243. [CrossRef]
86. Shah, J.M.; Li, Y.L.; Gessmann, T.; Schubert, E.F. Experimental analysis and theoretical model for anomalously high ideality factors ($n \gg 2.0$) in AlGaN/GaN p-n junction diodes. *J. Appl. Phys.* **2003**, *94*, 2627–2630. [CrossRef]
87. Liu, Y.; Cai, Y.; Zhang, G.; Zhang, Y.-W.; Ang, K.-W. Al-Doped Black Phosphorus p–n Homojunction Diode for High Performance Photovoltaic. *Adv. Funct. Mater.* **2017**, *27*, 1604638. [CrossRef]

88. Wang, C.-X.; Yang, G.-W.; Liu, H.-W.; Han, Y.-H.; Luo, J.-F.; Gao, C.-X.; Zou, G.-T. Experimental analysis and theoretical model for anomalously high ideality factors in ZnO/diamond p-n junction diode. *Appl. Phys. Lett.* **2004**, *84*, 2427–2429. [CrossRef]
89. Peng, T.-H.; Hong, C.-H.; Tang, M.-R.; Lee, S.-C. Photoresponse of homostructure WSe_2 rectifying diode. *AIP Adv.* **2019**, *9*, 075010. [CrossRef]
90. Afonso, J.; Leturcq, R.; Popa, P.L.; Lenoble, D. Transparent p-$Cu_{0.66}Cr_{1.33}O_2$/n-ZnO heterojunction prepared in a five-step scalable process. *J. Mater. Sci. Mater. Electron.* **2019**, *30*, 1760–1766. [CrossRef]
91. Lim, S.H.; Desu, S.; Rastogi, A.C. Chemical spray pyrolysis deposition and characterization of p-type $CuCr_{1-x}MgxO_2$ transparent oxide semiconductor thin films. *J. Phys. Chem. Solids* **2008**, *69*, 2047–2056. [CrossRef]
92. Narro-Ríos, J.S.; Garduño-Wilches, I.; Alarcón-Flores, G.; Ruiz-Rojas, C.A.; Gómez-Lizárraga, K.; Aguilar-Frutis, M. Spray pyrolysis synthesis of a semi-transparent p-$CuCrO_2$/n-ZnO heterojunction: Structural, optical, and electrical properties. *Phys. B Condens. Matter* **2022**, *624*, 413426. [CrossRef]
93. Avelas Resende, J. Copper-Based p-Type Semiconducting Oxides: From Materials to Devices. Ph.D. Thesis, Université Grenoble Alpes, Grenoble, France, Université de Liège, Liège, Belgium, 2017.